Under Pressure: Mechanochemical Effects on Structure and Ion Conduction in the Sodium-Ion Solid Electrolyte Na₃PS₄

Theodosios Famprikis,* Ö. Ulaş Kudu, James A. Dawson, Pieremanuele Canepa, François Fauth, Emmanuelle Suard, Mohamed Zbiri, Damien Dambournet, Olaf J. Borkiewicz, Houssny Bouyanfif, Steffen P. Emge, Sorina Cretu, Jean-Noël Chotard, Clare P. Grey, Wolfgang G. Zeier, M. Saiful Islam,* and Christian Masquelier*

ACCESS | Metrics & More | Article Recommendations | SI Supporting Information

ABSTRACT: Fast-ion conductors are critical to the development of solid-state batteries. The effects of mechanochemical synthesis that lead to increased ionic conductivity in an archetypical sodium-ion conductor Na₃PS₄ are not fully understood. We present here a comprehensive analysis based on diffraction (Bragg and pair distribution function), spectroscopy (impedance, Raman, NMR and INS), and *ab initio* simulations aimed at elucidating the synthesis−property relationships in Na₃PS₄. We consolidate previously reported interpretations regarding the local structure of ball-milled samples, underlining the sodium disorder and showing that a local tetragonal framework more accurately describes the structure than the originally proposed cubic one. Through variable-pressure impedance spectroscopy measurements, we report for the first time the activation volume for Na⁺ migration in Na₃PS₄, which is ∼30% higher for the ball-milled samples. Moreover, we show that the effect of ball-milling on increasing the ionic conductivity of Na₃PS₄ to ∼10⁻⁴ S/cm can be reproduced by applying external pressure on a sample from conventional high-temperature ceramic synthesis. We conclude that the key effects of mechanochemical synthesis on the properties of solid electrolytes can be analyzed and understood in terms of pressure, strain, and activation volume.
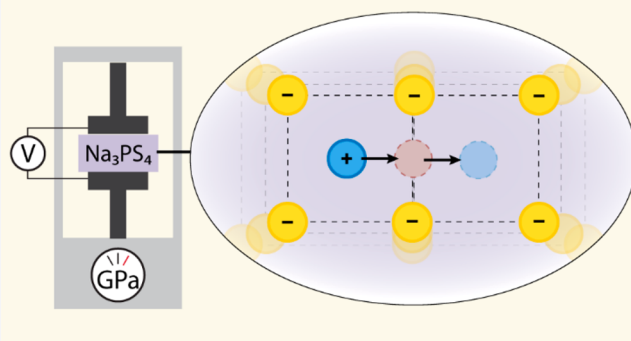
INTRODUCTION

Na₃PS₄ is an archetypical Na⁺ ion conductor in the thiophosphate family and of particular interest for the development of sodium solid-state batteries (SSBs). A tetragonal phase at room temperature (α, $P\bar{4}2_1c$) and a closely related cubic phase at $T > 250\ °C$ (β, $I\bar{4}3m$) have been described in earlier studies,[1] and we recently reported the existence of a third polymorph (γ, $Fddd$) with plastic crystal characteristics.[2] Na₃PS₄ synthesized through conventional high-temperature solid-state routes typically exhibits ionic conductivities of the order of 10^{-5} S/cm, which is somewhat low for SSB applications.[3] A resurgence of interest in Na₃PS₄ was initiated by Hayashi et al., who showed that the mechanochemical synthesis route (i.e., ball-milling) can lead to increased room-temperature ionic conductivities of the order of 10^{-4} S/cm, which allowed its integration into laboratory-scale SSB prototypes.[4−6] They proposed that this effect was due to the stabilization of the cubic β-phase as a result of ball-milling.

However, there is a discrepancy in the literature regarding the exact average structure of β-Na₃PS₄, with three different models proposed from the analysis of X-ray diffractograms.[7−9]

The difference between these models relates to the Na position(s) which have been described by either a fully occupied 6b site,[7] a 25% occupied 24f site,[8] or a combination of partially occupied 6b and 12d sites.[9] Considering the structure as an ionic-molecular crystal of Na⁺ and PS₄³⁻, it can be described as a body-centered cubic arrangement of the PS₄³⁻ anions (corners and center of the cell) in which all six-coordinated "interstitial" sites (centers of faces and edges) are occupied by Na⁺ (similarly to the intermetallic AuSb₃[10]). In this view, the latter "interstitial" sites for Na⁺ are described by the 6b position of the $I\bar{4}3m$ space group (Figure 1). The 12d and 24f sites then bridge the 6b sites, and their partial occupation can be interpreted as a sign of the Na⁺ diffusivity in the structure, tracing the diffusion pathways which are parallel
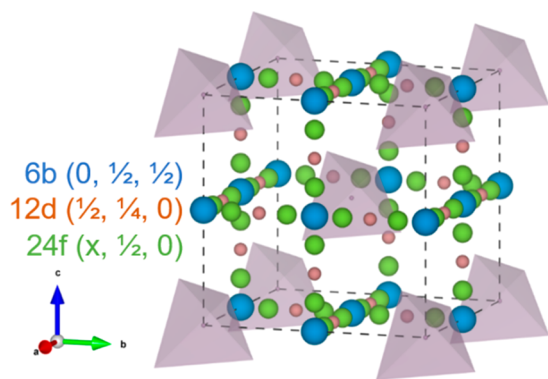
Figure 1. Distribution of Na$^+$ in β-Na$_3$PS$_4$ ($I\bar{4}3m$). PS$_4^{3-}$ moieties represented by purple tetrahedra and proposed Na$^+$ positions represented by spheres colored according to their respective Wyckoff site.

to the lattice vectors a, b, and c. The 12d site in particular is located at the midpoint between stable 6b sites and is considered as the "transition" site in the diffusion pathway.[9,11]

Nevertheless, the original hypothesis of the crystal structure (α vs β) significantly affecting ion conduction[4,5] has recently been challenged both experimentally and computationally: *ab initio* molecular dynamics simulations show similar diffusivity for Na$^+$ in both phases,[11–13] and pair distribution function (PDF) analyses reveal an identical local structure regardless of the sample preparation method.[7] We note that Hayashi et al. described the material in their related patent as "contain[ing] tetragonal Na$_3$PS$_4$".[14] Recent studies have also reported on tetragonal samples with conductivities up to 10^{-3} S/cm through quenching and/or annealing of ball-milled samples.[7,15]

The conductivity-enhancing effect of mechanochemistry is quite reproducible in Na$_3$PS$_4$,[16] and similar observations have been reported for several mechanically soft solid electrolytes (e.g., Li$_3$PS$_4$,[17] LiBH$_4$,[18] Ag$_3$PS$_4$,[19] Na$_{11}$Sn$_2$PSe$_{12}$,[20] and LiYCl$_6$[21]). However, the effect of mechanochemistry to produce highly conducting solid electrolytes remains poorly understood. Multiple hypotheses have been proposed including atomic-scale changes in crystal structure and/or in point defect concentrations, microstructural effects (such as grain boundaries), as well as mesostructural parameters such as particle size/shape and associated surface effects.[18,22,23] Both simulations and experiments show that introducing sodium ion defects through aliovalent doping can greatly enhance ion transport in Na$_3$PS$_4$.[9,11,13,24–30] Through novel atomistic simulations, the effect of grain boundaries on ion conduction in β-Na$_3$PS$_4$ has recently been examined,[31] showing that ion transport is not significantly affected by grain boundaries in this material in contrast to the sodium oxophosphate analogue.

Ball-milling synthesis consists in carrying out chemical reactions by application of mechanical force (mechanochemistry) in the form of collisions between the accelerated milling media (balls) and reagents.[32] In contrast to high-temperature ceramic synthesis where the energy input is thermal, in mechanochemical approaches the energy input is mechanical, i.e., pressure. The continually applied mechanical input can have side-effects on the resulting products, such as the reduction of particle and crystallite size as well as the accumulation of micro- and macrostrain. Despite the widespread use of ball-milling for the synthesis of soft solid electrolytes for batteries, the effects of particle size and strain on relevant functional properties have hardly been the subject of detailed investigation.

In this study, we explored the hypothesis of "mechanochemical" effects being the origin of the anomalously high conductivity of ball-milled Na$_3$PS$_4$ and related systems. We use this generic umbrella term to include all effects arising from the application of mechanical pressure (including mechanochemical synthesis) and capture the following features:

(a) Micro- and macrostrain on the local and average scales, respectively, which can dramatically affect the volume available for Na$^+$ diffusion and correlate with the activation volumes measured by pressure-dependent conductivity measurements.

(b) Effective interparticle contact which determines ionic percolation through solid electrolyte particles in a macroscopic pellet and can severely affect the measured ionic conductivity.

(c) Possible pressure-induced structural phase transitions.

Using a powerful combination of diffraction (Bragg and PDF), spectroscopic (impedance, Raman, inelastic neutron,
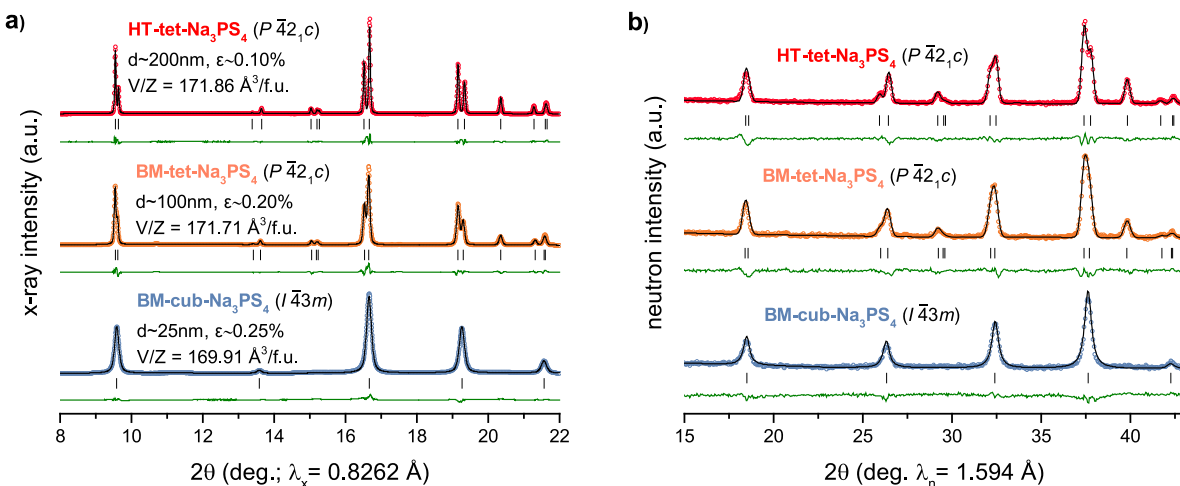

Figure 2. Sections of the synchrotron X-ray (a) and neutron (b) diffractograms of the Na$_3$PS$_4$ samples with associated Rietveld refinements. d and ε are the average isotropic crystallite size and average microstrain, respectively, extracted from analysis of the peak shapes of the X-ray data sets. Both panels compare the same q-range.

and nuclear magnetic resonance), and *ab initio* simulation techniques, we show that the main difference imparted on Na_3PS_4 by mechanochemistry is a distinct accumulated strain at both the local and average scales. This strain affects the dependence of the ionic conductivity on the applied pressure as quantified by a higher activation volume. Finally, we demonstrate that a key component to the conductivity increase ascribed to mechanochemistry is due to a mesostructural consolidation effect, increasing the effective interparticle contact area, which can be reproduced by a simple application of external pressure on a conventional high-temperature-synthesized sample.

RESULTS AND DISCUSSION

In the majority of our study, we compare two samples: a ground-state tetragonal α-Na_3PS_4 prepared by high-temperature solid-state synthesis (labelled here as HT-tet-Na_3PS_4) and a metastable cubic β-Na_3PS_4 prepared by ball-milling (BM-cub-Na_3PS_4). Inspired by previous work,[7,15] we also synthesized an "intermediate" sample prepared by rapid high-temperature annealing of a ball-milled sample, also resulting in tetragonal long-range symmetry (BM-tet-Na_3PS_4), which we invoke in certain parts of this paper. In agreement with previous studies, the ball-milled samples exhibit significantly higher room-temperature ionic conductivity (BM-tet and BM-cub, $\sim10^{-4}$ S/cm)[4−7,15,16] compared to the high-temperature-synthesized material (HT-tet, $\sim10^{-5}$ S/cm).[1,7,11,12,15]

Micro-, Average, And Local Structures of HT- and BM-Na_3PS_4. Synchrotron X-ray and neutron diffractograms confirm the purity of the products. The crystal structures could be accurately refined (Figures S1−S3) using starting models of Jansen and Henseler[1] for the tetragonal α-phase and of Nishimura et al.[8] for the cubic β-phase, respectively. The two phases are very closely related, with the phase transition involving the convergence of the lattice parameters, a slight orientational tilt of the PS_4^{3-} tetrahedra, and slight displacements of Na^+ to the middle of the edges and faces of the cubic cell. The close group−subgroup relationship between the two polymorphs[33] (Table S4) is evident in the diffractograms (Figure 2), which exhibit very similar features with characteristic merging and extinction of peaks from the tetragonal to the cubic phase.

From careful analysis of the X-ray Bragg diffractograms, we aimed at extracting microstructural parameters of the sample powders. Finite crystallite size and microstrain both cause peak broadening, which can be differentiated and quantified by analyzing the peak shapes (Lorentzian vs Gaussian) and widths as a function of the scattering vector (i.e., 2θ). The associated Williamson−Hall plot is given in Figure S4. Here, crystallite size refers to the average distance between coherent crystallographic domains in the powder, and microstrain refers to variation in the lattice parameters between such individual domains.

Figure 2 shows distinct peak broadening going from HT-tet to BM-tet to BM-cub, which we quantified as both a decrease in crystallite size and an increase in microstrain. The HT-tet sample shows a large crystallite size of ~200 nm with a negligible average microstrain of $\sim0.1\%$, while the analysis of the BM-cub sample results in a minimal grain size of ~25 nm with a significant microstrain of $\sim0.25\%$. These microstructural differences can be attributed to the different synthesis routes: high-temperature annealing results in grain growth and strain release, while high-energy ball-milling subjects the sample to

sizable mechanical forces and frequent impact, resulting in crystallite fracture and strain accumulation. It is interesting to note that the "intermediate" sample BM-tet exhibits a larger crystallite size (~100 nm) but rather high microstrain ($\sim0.2\%$, similar to BM-cub). We conclude here that the rapid 20 min annealing of the ball-milled sample leads to some grain growth but is not sufficient to significantly relieve the microstrain induced by ball-milling. We attempted to corroborate these results by transmission electron microscopy but were impeded by the well-known instability of thiophosphates under the high electron doses required for high resolution imaging.

In addition, the observed microstrain seems to also be associated with compressive macrostrain, i.e., a shrinkage of the average lattice volume observable from diffraction peak positions. An inspection of the superimposed PDFs of the samples (Figure S5) and their refinements (Figures S6−S8), extracted by total scattering experiments, is consistent with the Bragg diffractograms: the two tetragonal samples (HT-tet, BM-tet, indexed in $P\bar{4}2_1c$) largely coincide, while the BM-cub (indexed in $I\bar{4}3m$) shows distinct deviations and shifts to a lower interatomic correlation distance, which indicates the shrinkage of the cell. From refinements of the Bragg and PDF data sets, the lattice volume decreases from 171.9 (172.7) to 171.7 (172.3) to 169.9 (170.7) Å^3 per formula unit from HT-tet- to BM-tet- to BM-cub-Na_3PS_4, respectively. We note that volume variations could be indicative of variations in the mobile defect concentrations as Na vacancies are expected to cause local contraction of the lattice. Alternatively, the reduction in volume could be associated with the dramatically reduced crystallite size and corresponding increase in surface tension of these crystallites. We conclude that the mechanical energy input during the ball-milling synthesis reduces the particle and crystallite sizes of the resulting powder and also imparts a micro- and macrostrain on the structure of the resulting crystal.

In order to explain the stabilization of the average cubic structure after ball-milling, we have investigated the relative phase stability of the α- and β-polymorphs as a function of pressure using density functional theory (DFT) calculations. Consistent with experimental observation, the cubic β-polymorph has a higher formation energy and smaller equilibrium volume (Figure S9 and Table S11) than the tetragonal α-phase in the absence of applied pressure. Using the DFT-calculated values for energy (E), volume (V), and pressure (P), we calculated the enthalpy of formation ($H = E + PV$) for each polymorph as a function of the applied pressure. As the pressure increases, the lattice parameters of the tetragonal phase converge to the same value, and the (absolute) difference in enthalpy between the two polymorphs decreases, indicating a stabilization of the cubic polymorph (Figure 3). The enthalpy difference approaches zero in the range 10−15 GPa, and as such, a pressure-induced phase transition from tetragonal to cubic is predicted in this pressure range. We conclude that the apparent stabilization of the cubic β-polymorph for the BM-cub sample can be understood as a result of the mechanical stress applied on the sample during the mechanochemical synthesis. In situ variable-pressure diffraction experiments are scheduled to experimentally confirm this computationally predicted pressure-induced phase transition of Na_3PS_4.

Next, we utilized Rietveld-type refinements of our diffraction data to probe the precise Na-ion distribution in BM-cub-Na_3PS_4. Variations in the possible sodium positions (see
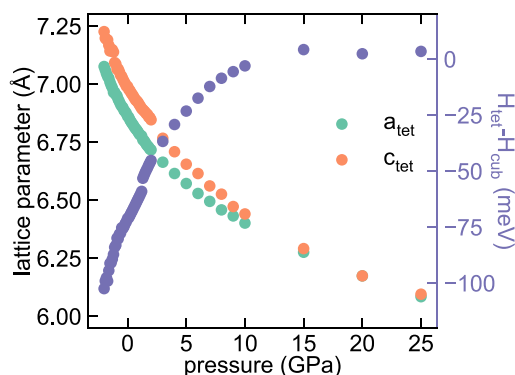
Figure 3. Variation of the calculated lattice parameters of α-Na$_3$PS$_4$ (green and orange) and the difference in enthalpy (in violet) between α- and β-Na$_3$PS$_4$ as a function of pressure.

Figure 1) yield small differences of the peak intensities of Bragg diffractograms, which is why we complemented this analysis with total scattering. On this basis, we have attempted numerous fits of our three diffractograms of BM-cub-Na$_3$PS$_4$ (X-ray Bragg, neutron Bragg, and X-ray total scattering) in inverse- and direct-space (Rietveld and PDF, respectively) in the cubic $I\bar{4}3m$ framework in an effort to resolve the controversy. The results are tabulated in Table S12 and rationalized below. We find that the majority of Na scattering density is centered around the 6b site but appears to be

nonspherical, probably owing to the directionality of Na$^+$ conduction through the lattice. Splitting the 6b site into a partially filled 24f site (with x close to 0) helps to better capture this anisotropy as does fitting anisotropic (ellipsoidal) thermal displacement parameters. Neither inverse- nor direct-space analyses reveal signs of significant occupation of the 12d "transition" site alone or in partial occupation, in agreement with the conclusions of Krauskopf et al.[7] The model that best reconciles all diffraction data sets is one with a 25%-occupied 24f site ($x \approx 0.05$) with anisotropic displacement parameters. This is in good agreement with the interpretation of Nishimura et al. for a β-Na$_3$PS$_4$ sample measured at 600 K[8] and indicative of directional mobility of Na$^+$ in this structure.

In contrast to their interpretation from X-ray Bragg diffraction,[4,5] Hayashi et al., following their seminal report on the mechanochemical synthesis of "cubic" Na$_3$PS$_4$, filed an associated patent describing the material as "containing tetragonal Na$_3$PS$_4$",[14] without, however, further substantiation of that description. A close inspection of the synchrotron X-ray diffractogram of BM-cub-Na$_3$PS$_4$ (Figure 4a) reveals weak, broad peaks, unindexed by the cubic $I\bar{4}3m$ space group of β-Na$_3$PS$_4$, which correspond well to the expected peaks for the tetragonal $P\bar{4}2_1c$ space group of α-Na$_3$PS$_4$ for $a \approx c$. In particular, the (102), (212), (203), (322), and (104) families of peaks of $P\bar{4}2_1c$ are observable. These peaks are only observable in a primitive cell and would not be indexed in a body-centered tetragonal space group, e.g., $I\bar{4}2m$ as proposed
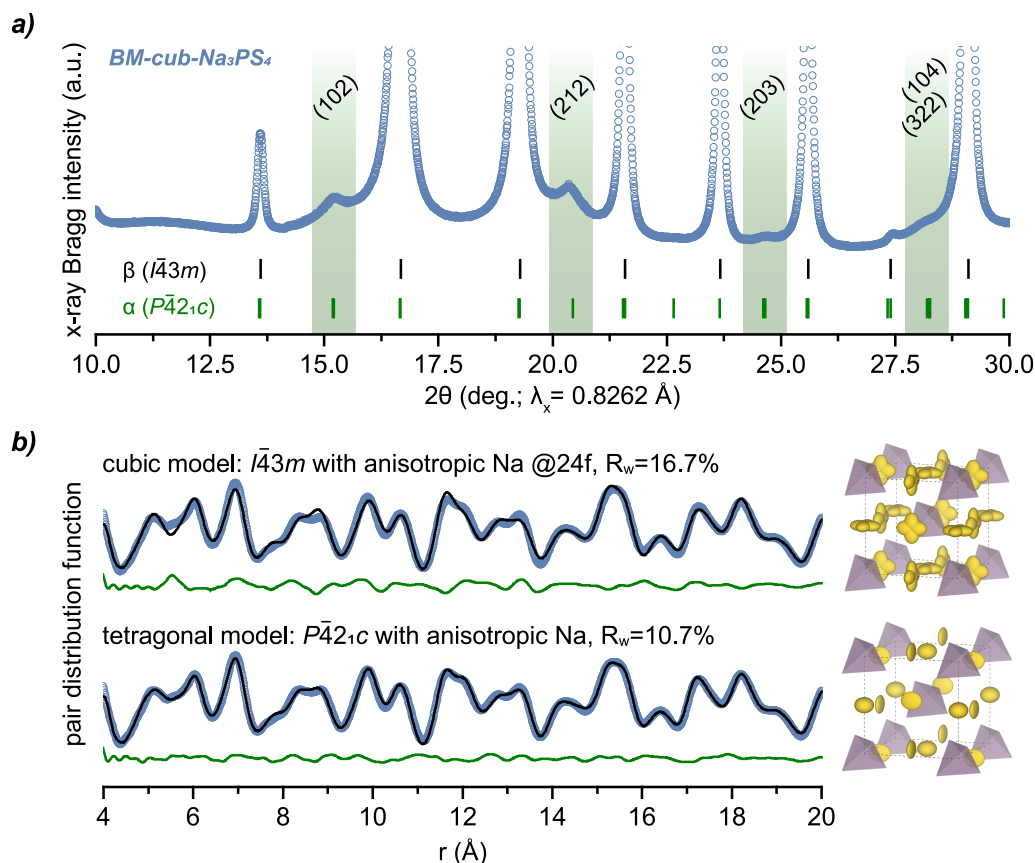

Figure 4. (a) Highlighted weak unindexed "tetragonal" peaks in the Bragg diffractogram of BM-cub-Na$_3$PS$_4$. (b) Comparison of the PDF fits of BM-cub-Na$_3$PS$_4$ using cubic and tetragonal average symmetry with visualizations of the resulting structural models. PDF refinements were performed for a symmetry-confined, single-unit-cell in the range 4−20 Å and in both cases $a \approx c \approx 6.99$ Å. Displacement ellipsoids represented at 90% probability.

recently by Seidel at al.[33] We are not the first to measure this; practically every diffractogram of ball-milled "cubic" Na_3PS_4 reported in the literature features these reflections.[4−7,9,11,14−16,30,34] However, this observation has never been adequately explained: it is unclear whether these reflections originate from a secondary tetragonal phase, are indicative of a tetragonal average structure, or originate from partial ordering of the main phase.

Recently, Krauskopf et al. remarked that the local structure of the BM-cub sample is better described by an average tetragonal model, highlighting a discrepancy between average and local structures observable by Bragg and total scattering diffraction experiments, respectively.[7] Our symmetry-confined PDF analysis of a single-unit-cell, shown in Figure 4b, confirms this observation: the refinement of the local structure of the BM-cub sample from PDF analysis in the $P\bar{4}2_1c$ tetragonal space group (R_w = 10.7 %) results in a much better fit of the data compared to those in the cubic $I\bar{4}3m$ space group (Table S5, R_w > 16.7 %) for the range 4−20 Å (see comment regarding the exclusion of first neighbors in the Methods section). We note that in both cases the anisotropy of the Na^+ density around the Na position is evident from the PDF fits (structure visualizations in Figure 4b).

Spectroscopy Analysis of Local Structures. Vibrational spectroscopy experiments were performed to further probe the local structure of the Na_3PS_4 samples. The measured Raman spectra (Figure 5a) reveal no differences between the three Na_3PS_4 samples (apart from a distinct fluorescence of the BM-cubic sample which lies outside the scope of this study). At room temperature, the spectra are dominated by the four internal normal modes of the thiophosphate tetrahedral polyanions as indexed in Figure 5a ($\nu_1 \sim$ 412, $\nu_2 \sim$ 214, $\nu_3 \sim$ 535, $\nu_4 \sim$ 280 cm^{-1}). A distinct splitting of the normal modes is observed, especially in the asymmetric stretching and bending modes, ν_3 and ν_4, respectively. This splitting is indicative of deviations from the ideal tetrahedral (T_d) symmetry of the PS_4^{3-} moiety and can correlate to the point group symmetry of the phosphorus site in the crystal structure. Indeed, in the cubic $I\bar{4}3m$ description, the phosphorus occupies the 2a Wyckoff position with $\bar{4}3m$ (T_d) point group symmetry, while, in the tetragonal $P\bar{4}2_1c$ description, the phosphorus occupies the 2a Wyckoff with point group symmetry $\bar{4}(S_4)$. In other words, the internal vibrations of the PS_4^{3-} unit in the tetragonal space group are slightly distorted due to the absence of the ideal T_d point symmetry.

To further rationalize this observation, we simulated the vibrational frequencies/energies for the two polymorphs using DFT, as shown in Figure 5b. The calculations indicate that there should be significant differences between the α- ($P\bar{4}2_1c$) and β- ($I\bar{4}3m$) polymorphs in agreement with our experimental observations. If the local structure of the BM-cub sample were truly cubic, singlet peaks should be observed at 535 and 280 cm^{-1}, associated with the ν_3 and ν_4 modes, respectively, and the symmetric P−S stretching mode (ν_1) at 412 cm^{-1} should be appreciably shifted, neither of which is the case. In all spectra, we observe invariantly the splitting of the PS_4^{3-} normal modes indicating the same non-cubic local structure for all samples, including the BM-cub sample. These observations are consistent with the PDF interpretation and also in agreement with all reported Raman spectra for ball-milled Na_3PS_4 samples in the literature.[16,35]

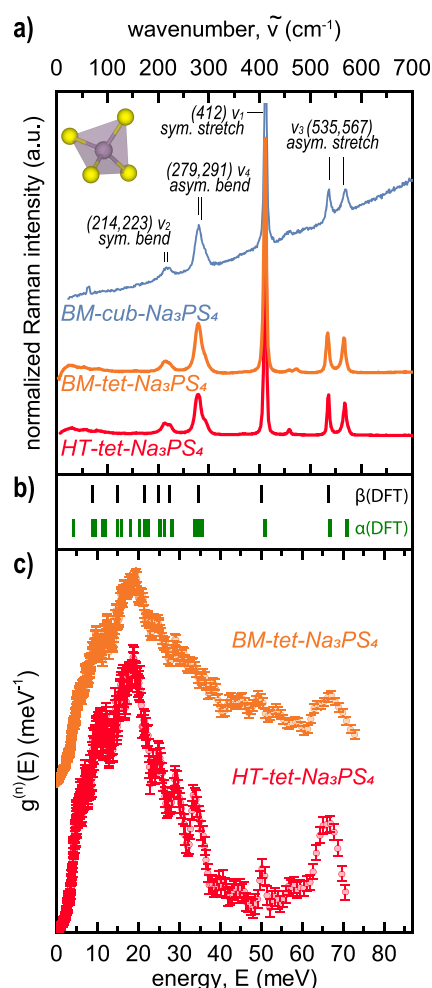Vibrational modes below 200 cm^{-1} (~25 meV) are not fundamental but relate to interactions of the anionic and

Figure 5. Phonon spectra of the Na_3PS_4 samples. (a) Raman spectra measured at room temperature. (b) DFT-calculated vibrational frequencies/energies at the γ-point based on the published α and β structural models ($P\bar{4}2_1c$ and $I\bar{4}3m$, respectively). (c) Phonon spectra, in terms of generalized density of states (GDOS) extracted from inelastic neutron scattering measurements at room temperature. The x-scales in all panels are matched ($E = hc\tilde{v}$).

cationic lattices. Presumably, owing to the high mobility of Na^+ in Na_3PS_4, these modes are broadened and not observable in the Raman spectra at room temperature. However, such modes are well observed in the generalized phonon density of states (GDOS) extracted from inelastic neutron scattering measurements (INS, Figure 5c). This is because the INS-measured GDOS involves a weighting of the scattering ions with their scattering power. A distinct broadening of the low-energy modes in the GDOS is observed for the ball-milled sample, which can be attributed to the dynamical signature of local mobility and disorder incurred by mechanochemical synthesis. Further, the mode around 65−70 meV of the GDOS, corresponding to the ν_3 asymmetric P−S stretch, seems to be more separated in the BM sample, and the peak at ~50 meV corresponding to the ν_1 symmetric P−S stretch is significantly dampened. These observations could relate to the observed microstrain and high thermal displacement parameters for P and S made evident by diffraction (Tables S1−S3) and could be interpreted to indicate further local deviations of the PS_4^{3-} units from ideality.

The local environment of Na and P atoms can be further elucidated through MAS NMR spectroscopy. The ^{23}Na spectra in Figure 6a show that the sodium ion environments in the
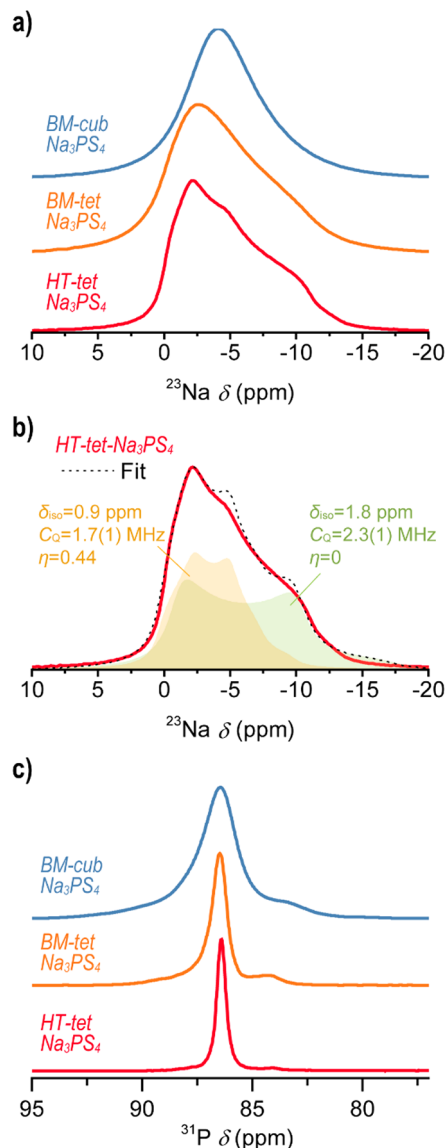

Figure 6. Room-temperature MAS NMR spectra of the Na_3PS_4 samples. (a) ^{23}Na spectra exhibiting lower quadrupolar broadening and more symmetrical resonance with ball-milling. (b) Example fit of the ^{23}Na spectrum for HT-tet sample indicating two Na environments. (c) ^{31}P spectra of the Na_3PS_4 samples exhibiting higher broadening of the main PS_4^{3-} peak at ~86 ppm with ball-milling.

HT-tet and BM-tet samples are similar, featuring a distinct quadrupolar line shape, which can be fitted using the same quadrupolar NMR parameters with varying line broadening. The fit of the HT-tet spectrum yields two signals with δ_{iso} = 1.8 and 0.9 ppm, C_Q = 2.3(1) and 1.7(1) MHz, and η = 0 and 0.44, respectively (Figure 6b). While C_Q values are in line with previous measurements,[26] there is some uncertainty in the fitting of δ_{iso} and η. Similar fits were performed on spectra obtained at two additional field strengths (9.4 and 16.4 T in addition to 11.8 T shown here) for HT-tet and show good agreement for the same quadrupolar parameters (Figure S10 and Table S13). The less distinct features of the BM-tet

spectrum are consistent with a greater distribution of quadrupolar environments, as expected from a more disordered sample (smaller crystallite size, higher microstrain, and a distribution of local environments).

The spectrum of BM-cub-Na_3PS_4 contains a more symmetrical and narrower resonance with a chemical shift close to the center of mass of the other two spectra. This is consistent with motional averaging and higher Na-ion mobility: Yu et al.[11] have shown that at lower temperatures a quadrupolar line shape is still visible for the cubic phase, and a transition to a more Gaussian line shape occurs between 293 and 398 K or 313 and 353 K for static or MAS NMR, respectively. The narrower line shape observed here at lower temperatures is ascribed to a combination of higher mobility and the higher magnetic field strengths used here, i.e., not 9.4 T but 11.8 T. The latter results in smaller second-order quadrupolar broadening, and thus, the onset spectral narrowing occurs at lower hopping frequencies.

The characteristic ^{31}P signal for the PS_4^{3-} anion at ~86 ppm shows moderate (BM-tet) or significant (BM-cub) broadening for the ball-milled samples compared to the HT-tet-Na_3PS_4 sample (Figure 6c). This is consistent with the local disorder and the extensive strain evident from the preceding analysis. The significant broadening for the BM-cub sample indicates much higher disorder and a distribution of local environments causing a wider range of chemical shifts. In order to definitively distinguish between static or dynamic disorder, additional variable-temperature NMR would be required. The small signal around 84 ppm has previously been assigned to PS_4^{3-} (and PS_3O^{3-}) units in a glassy environment,[26] and there are many possible impurities with a lower shift; e.g., various glassy and crystalline phases in the $Na_2S-P_2S_5$ system could cause the resonances of the PS_4^{3-} anions to be shifted to lower frequencies than in the Na_3PS_4 end member (in analogy to studies of the $Li_2S-P_2S_5$ system[36]). Surprisingly, the shift is constant for both tetragonal phases, while the signal shifts to ~83 ppm for the cubic phase suggesting the possibility that the peak originates from a defect within the Na_3PS_4 and is thus affected by the processing conditions. The higher frequency shoulder is tentatively assigned to connected PS_4-tetrahedra, e.g., $P_2S_7^{4-}$ as similar resonances have been observed in $Li_2S-P_2S_5$ glasses.[37] $P_2S_7^{4-}$ units could result, for example, from S^{2-} vacancies in Na_3PS_4.

The combination of thorough diffraction and spectroscopy analyses on HT- and BM-Na_3PS_4 converges to the following comparative observations: they possess (i) the same tetragonal local structure (PDF, Raman) irrespective of the synthesis method and (ii) a distinct disorder induced by ball-milling which can be quantified with significantly higher displacement parameters for all atoms (Bragg diffraction, PDF) and which leads to the observation of a more symmetric average structure (Bragg diffraction, NMR). It is conceivable that multiple domains of coherent tetragonal distortion are distributed in each crystallite of "cubic" BM-cub-Na_3PS_4. Additionally, the data suggest a rotational disorder of the PS_4^{3-} units (NMR, INS), which are likely statistically distributed in a static manner.

Variable-Pressure Ionic Conductivity and Activation Volumes. The variation of ionic conductivity with applied pressure is of significant interest from both a fundamental and a practical point of view. Practically, it is widely recognized that applying pressure plays a key role on the electrochemical cycling of solid-state batteries, and most successful lab-scale

proofs-of-concept utilize custom-made setups to effectively measure and control pressure.[38−41] More fundamentally, pressure as a thermodynamic variable can affect the ion dynamics of materials which, in turn, dictate functional properties such as ionic conductivity. In analogy to the activation energy for ion conduction, E_a, which describes the evolution of ionic conductivity with temperature through an Arrhenius-type relation (eq 1), a characteristic activation volume for conduction, V_a, can describe the evolution of ionic conductivity with applied pressure.[42−53] The two activation parameters E_a and V_a are linked in that the activation volume describes the evolution of activation energy with pressure (eq 2):

$$E_a = -k_B \left(\frac{\partial \ln(\sigma T)}{\partial T^{-1}} \right)_P \tag{1}$$

$$V_a = \left(\frac{dE_a}{dP} \right)_T = k_B T \left(\frac{\beta}{3} - \frac{\partial \ln(\sigma)}{\partial P} \right)_T \tag{2}$$

where k_B is the Boltzmann constant, and β is the material compressibility (the inverse of the bulk modulus). The derivation of eq 2 is shown in the Supporting Information (eqs S3−S14). Activation volumes are typically reported in cm^3/mol but can be converted to $Å^3$ through the Avogadro constant to be directly compared with crystallographic volumes. Reported data of activation volumes of inorganic, cation conductors in the literature are summarized in Table 1. Evidently, there is a distinct lack of such data, especially in recent studies dealing with high-performance, room-temperature Li^+ and Na^+ conductors aimed at SSB applications.

The activation volume is often physically interpreted as a local volume *change* in the atomic structure of the material associated with ion migration[48,54] and can be considered as the difference between the volume required for ion migration (V_m) and the free volume already available in the structure (V_f):

$$V_a = V_m - V_f \tag{3}$$

This interpretation is elegantly demonstrated in the example of the beta aluminas[46] (Table 1). For Na-β-Al$_2$O$_3$, the activation volume is ~0, indicating facile Na^+ conduction through 2D channels in between the alumina planes ($V_m = V_f$). For the larger K^+ and Rb^+, the activation volume increases because the alumina planes need to expand to allow the larger alkali ions to migrate ($V_m > V_f$). On the other hand, in Li-β-Al$_2$O$_3$, the smaller Li^+ is coordinated more strongly and closer to one of the planes rather than in between. Hence, in order for Li^+ to get to the migration pathway the planes need to contract, giving rise to a negative activation volume ($V_m < V_f$). In the framework of this interpretation, the activation volume is characteristic of the migration mechanism. The example of the beta aluminas also demonstrates that a lower activation volume does not necessarily lead to higher ionic conductivity. Even with a negative activation volume, Li-β-Al$_2$O$_3$ shows a much lower ionic conductivity compared to Na-β-Al$_2$O$_3$.[46] Nevertheless, negative activation volumes seem to be a characteristic of certain Ag^+ conductors (see Table 1), in which case it might be related to their superionic nature, i.e., the unimpeded flow of ions through abundant unoccupied sites[43] and/or the negative thermal expansion coefficient exhibited by these materials.[42] In that sense, it is crucial that the activation volume should be interpreted in the framework of the specific structure and migration mechanism.

Table 1. Values of Activation Volume for Cation Conduction in Inorganic Solid Electrolytes in the Literature

compound	temperature (°C)	activation volume (cm³/mol)	ref.
β-AgI	21	−5.9 ± 0.5	42
γ-AgI	21	−3.6 ± 0.6	42
Ag$_3$SI	30	−2.3 ± 0.4	43
Ag$_3$SBr	30	−1.2 ± 0.6	43
RbAg$_4$I$_5$	18	−0.32	44
α-AgI	382	0.9	45
Li-β-Al$_2$O$_3$	23	−0.7	46
Na-β-Al$_2$O$_3$	23	~0	46, 47
K-β-Al$_2$O$_3$	23	1.3	46
LiBH$_4$	220	4.6	48
Li$_{0.95}$Ca$_{0.025}$BH$_4$	220	3.2	48
Li$_{0.35}$La$_{0.52}$TiO$_3$	−35 to 21	1.6−1.7	49
α-Li$_2$SO$_4$	650	0.51	50
Li$_{16−2x}$Zn$_x$(GeO$_4$)$_4$ (x = 1, 2)[a]	27	0.26, 0.58	51
Li$_{3+x}$Ge$_x$V$_{1−x}$O$_4$ (x = 0.25, 0.6, 0.72)[a]	27	6.00, 4.34, 4.00	51
Na$_{1+x}$Zr$_2$Si$_x$P$_{3−x}$O$_{12}$ (x = 1.8−2.3)	300	3.0−1.6	52
Na$_3$SbS$_4$	(RT)	1.20 ± 0.08	53[b]
BM-cub-Na$_3$PS$_4$	23	2.33 ± 0.04	this work
HT-tet-Na$_3$PS$_4$	23	1.78 ± 0.02	this work

[a]These materials did not show monotonic behavior with increasing pressure, and the activation volume listed refers to the "low-pressure" regime; see cited references. [b]Extracted in this work from literature data; see Figure S13 and Table S16

In order to determine the activation volume for Na$_3$PS$_4$, we performed impedance spectroscopy measurements on pelletized samples as a function of in situ applied pressure within a uniaxial hydraulic press. Similar to variable-temperature experiments, these measurements lead to a significant evolution of the electrical response, as shown in Figure 7a,b for the BM-cub and HT-tet samples, respectively. From the impedance spectra we extract the ionic conductivity of the samples (Figure 7c) through fitting of equivalent circuits composed of resistors and constant phase elements. Two critical observations emerge, which can be used to clarify the synthesis−property relationships of Na$_3$PS$_4$:

(i) The HT- and BM-synthesized samples differ decisively in their intrinsic evolution of ionic conductivity with applied pressure, as precisely quantified by their activation volumes.

(ii) Both HT- and BM-synthesized samples exhibit the same order of magnitude of ionic conductivity ($10^{−4}$ S/cm) under pressure, in contrast to their ~10-fold difference when measured ex situ. This effect is independent from the intrinsic activation volume and discussed separately.

The impedance spectra of the BM-cub-Na$_3$PS$_4$ sample can be described with a single diffusion process (one semicircle in Figure 7a). The extracted capacitance using the Brug relationship[55] is in the order of $10^{−10}$ F and clearly identifies the origin of this conductivity as intragrain ion migration. In contrast, the spectra of the HT-tet-Na$_3$PS$_4$ sample can be better described by two diffusion processes (two semicircles in Figure 7b). The two impedance contributions yield significantly different ω_{max} by ~1 order of magnitude, but their
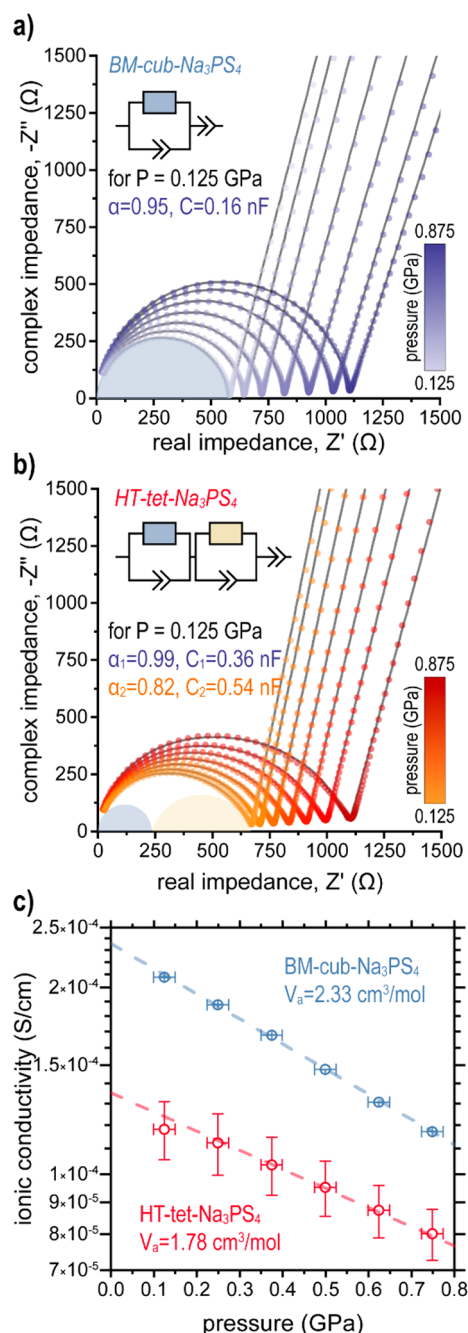
Figure 7. In situ variable-pressure impedance spectroscopy experiments. Spectra collected in the direction of pressure release as a function of applied uniaxial pressure in Nyquist coordinates and associated equivalent circuit fits of HT-tet-Na_3PS_4 (a) and BM-cub-Na_3PS_4 (b). (c) Variation of ionic conductivity with pressure for BM-cub- and HT-tet-Na_3PS_4 quantified by their respective activation volumes.

extracted capacitances are in the same order of magnitude (10^{-10} F). It is unclear at this point if these two impedance contributions can be ascribed to intra- and intergrain diffusion processes, respectively. We note, however, that the respective evolution of the resistances of the two processes shows approximately the same evolution with pressure (i.e., activation volume). As such, we use their sum in their following analysis to represent the total conductivity of HT-tet-Na_3PS_4.

In all cases, after initial pressing, the conductivity of Na_3PS_4 samples was shown to monotonically decrease with increasing pressure. The evolution of conductivity can be well described with a constant negative slope between the logarithm of conductivity and pressure $\left(\frac{\partial \ln(\sigma)}{\partial P}\right)_T$ as shown in Figure 7c. A distinct difference in slope is observable between the BM-cub- and HT-tet-Na_3PS_4 samples: the conductivity of the ball-milled sample is more sensitive to the applied pressure. Following eq 2, the observed slope in Figure 7c was corrected using the compressibility of Na_3PS_4 to derive the activation volume. It should be noted that the compressibility of a macroscopic object (pellet) is dependent on its micro- and mesostructure and especially on the presence of porosity. Unfortunately, our experimental setup did not allow for the in situ quantification of the density of each sample; however, cold pressing (HT or BM) Na_3PS_4 routinely results in >95%-dense self-standing pellets after application of moderate pressures (~300 MPa). As such, in the following analysis, we have assumed that the samples exhibit full densification in the in situ configuration and hence the same bulk modulus $B \approx 25$ GPa (i.e., $\beta \approx 0.04$ GPa^{-1}), which is an average among our calculations and literature values[56−59] (Table S14). We note that if densification of the Na_3PS_4 powders was still taking place, the exhibited slopes in Figure 7c should deviate from linearity, and the capacitances derived from fitting the impedance spectra (Figure S12) would significantly evolve, neither of which is the case. Under this reasonable assumption, the compressibility correction accounts for <10% of the observed variation of ionic conductivity with pressure (Table S15 and Figure S11). We conclude that the activation volume for Na$^+$ conduction in the BM-cub sample is 2.33 cm^3/mol, larger by ~30% than the value of 1.78 cm^3/mol for the HT-tet sample (while BM-tet samples exhibited intermediate values).

In the Na_3PS_4 structure, ion hops occur between the stable lattice sites (6b in the $I\bar{4}3m$ description of Figure 1) parallel to the cell edges[13,60] as illustrated in Figure 8 for a jump along the a-direction ([100]). Between each pair of lattice sites, a four-coordinated site acts as the metastable transition site for ion migration (12d in the $I\bar{4}3m$ description of Figure 1). In Na_3PS_4, stable lattice sites have an average Na−S bond length of ~2.86 Å corresponding closely to the average Na^{IV}−S bond of 2.84 Å tabulated by Shannon.[61] In contrast, the average Na−S distance at the transition state is significantly shorter (~2.65 Å). In order for ion hops to occur, the bottleneck separating the stable site from the transition state needs to expand to allow the Na ions to transverse it, and the observable activation volume can be interpreted as a measure of this necessary local expansion to allow for ion migration (~3 Å^3 for HT-tet-Na_3PS_4). Applied pressure acts against this necessary expansion increasing the activation energy by V_aP (eq 2) and thus reducing the ionic conductivity. In other words, the decrease in conductivity under applied pressure can be attributed to stiffening of the transition states ("bottlenecks"), effectively increasing the energy barrier for successful ion hops.

The significant difference in activation volume between BM-cub-Na_3PS_4 and HT-tet-Na_3PS_4 can be rationalized on the basis of variations in the available volume for conduction (V_f in eq 3). The distinct macro- and microstrain observable from diffraction lead to a decrease in the available volume for Na$^+$ to migrate in the structure. The 0.55 cm^3/mol (0.90 Å^3) difference in activation volume from the variable-pressure impedance measurements can be interpreted as this decrease
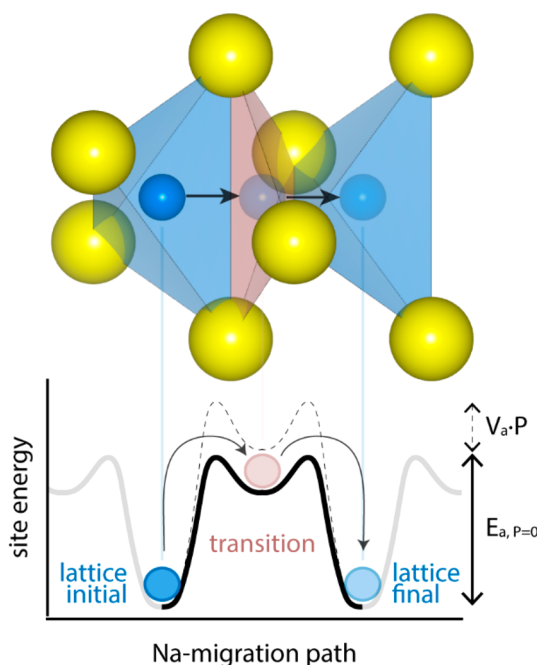
Figure 8. Schematic representation of the ion-hopping topology in Na_3PS_4 parallel to [100] with the associated energy landscape. The transition site (bottleneck) needs to expand to allow for Na^+ hops between the lattice sites. Applied pressure acts against this expansion, increasing the activation energy for migration, as indicated by the dotted lines.

in available volume for ion conduction owing to the strain incurred by the mechanochemical synthesis method. This value is directly comparable to the difference in average lattice volume of ~2 Å^3 per formula unit of Na_3PS_4 determined by diffraction (see Figure 2).

It is also interesting to compare our results for the activation volume of Na_3PS_4 with results for isostructural compounds. Using the recently reported data sets of Wang et al. for variable-pressure diffraction and impedance spectroscopy,[53] we derive a bulk modulus of 46 GPa and an activation volume of 1.20 cm^3/mol for Na_3SbS_4 (Figure S13 and Table S16). This activation volume is $\sim25\%$ lower than that of HT-tet-Na_3PS_4.

Substitution of Sb in the Na_3PS_4 structure causes the unit cell volume to expand by $\sim9\%$ (from ~170 to ~185 Å^3/f.u.). The majority of this volume difference can be attributed to the larger SbS_4^{3-} tetrahedron but the substitution also creates significantly more free volume, V_f, accessible for Na^+ diffusion. This interpretation is qualitatively consistent with a lower activation volume for Na_3SbS_4, whose lattice would have to expand to a smaller degree to allow Na^+ diffusion compared to Na_3PS_4. Similarly, we expect the larger, isostructural Na_3PSe_4[12,62−64] and Na_3SbSe_4[63,65] to present even lower activation volumes.

Figure 9a compares the impedance spectra of the HT-tet-Na_3PS_4 sample before and after the variable-pressure experiments, showing a ~10-fold increase in ionic conductivity. Before the variable-pressure experiments, the pellet of Na_3PS_4 (prepared at ~625 MPa) exhibited a conductivity of $\sim10^{-5}$ S/cm, typical for a high-temperature synthesized sample.[1,7,11,12,15] A second resistive component is observable (second semicircle in the Nyquist plot) exhibiting a capacitance in the 10 nF range, which we associate with ion transfer between particles. After the variable-pressure experiments, the electrical signal significantly changes, the two phenomena merging in essence into a single ion-transport phenomenon attributable to intragrain diffusion and severely decreased resistance. The full chronological data set of the variable-pressure conductivity of HT-tet-Na_3PS_4 is presented in Figure S14.

Similar observations of increased conductivity upon pressing were found from recent variable-pressure conductivity measurements on the isostructural Na_3SbS_4.[53] These observations are analogous to variations of measured ionic conductivity as a function of pellet preparation which has been reported for several solid electrolytes,[66−68] including ball-milled Na_3PS_4.[57] We attribute this to extrinsic effects on macroscopic ionic percolation through the consolidation of the pellet, improving particle−particle and pellet−electrode contact (in contrast to the intrinsic material response to applied pressure capture by the activation volume). Figure 9b schematically demonstrates this effect: when a solid electrolyte powder is pressed into a pellet, limited particle−particle contact can severely reduce the effective area available for ion
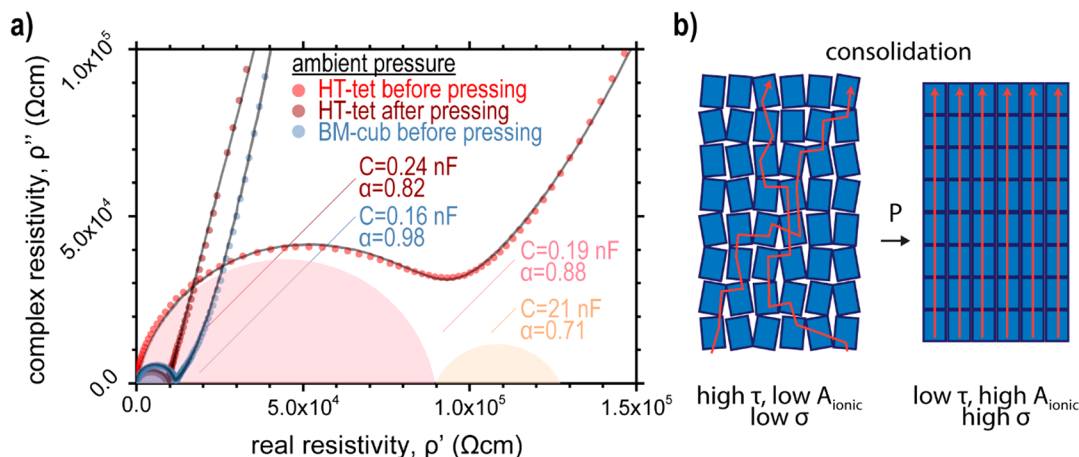

Figure 9. (a) Comparison of the ambient pressure impedance spectra of HT-tet-Na_3PS_4 and BM-cub-Na_3PS_4 before and after the variable-pressure experiment in Nyquist coordinates. Data normalized by sample dimensions. (b) Schematic representation of mesoscopic consolidation leading to higher observable conductivity after pressing. Blue rectangles indicate solid electrolyte particles, and red lines indicate paths of least resistance for conducting ions. τ, A_{ionic}, and σ denote tortuosity, effective area for ion transport, and ionic conductivity, respectively.

transport (A_{ionic}), forcing all ions to pass through limited mesostructural bottlenecks. In addition, tortuosity (τ) is introduced, increasing the effective distance that ions have to transverse between electrodes. Both of the above effects lead to a significant reduction of the observable ionic conductivity. We underline the difference between the proposed consolidation mechanism and "densification", which would refer to significant change in porosity and the overall density of the pellet. In our view, densification alone cannot explain the experimental observations since pellets of Na_3PS_4 prepared under the conditions used here present a >95% compactness already before the variable-pressure experiments. On the contrary, the increase of particle contact by consolidation can take place without appreciable change in the overall density of the pellet.

Furthermore, we highlight that such an effect of consolidation upon in situ pressure application was not evident for the BM-Na_3PS_4 sample. We hypothesize that the significantly smaller particle size of the ball-milled sample allows for its facile consolidation already upon pellet formation and thus much easier access to the full potential of the material in terms of macroscopic ionic conductivity. This effect alone can account for the majority of the observed differences in the literature between HT- and BM-synthesized samples, which have been previously ascribed to the introduction of mobile defects. Nevertheless, the fact that the ball-milled samples are still slightly more conducting (despite their higher activation volume) means that the defect introducing nature of ball-milling cannot be discarded as a parallel influence on ion transport.

Through our observations on Na_3PS_4, our study highlights some limitations of the current commonplace approaches to probing the performance of solid electrolytes. In particular, impedance spectroscopy on pelletized samples largely depends on the procedure of pellet preparation, and the conductivities measured should not necessarily reflect the intrinsic behavior of the material on the atomic scale. Impedance spectroscopy experiments performed at low temperatures[66,69] and/or on single-crystals[70,71] can help to distinguish or eliminate the microstructural effects, respectively, thus revealing the "real" intrinsic ion transport on the atomic scale. Furthermore, we hope to inspire further variable-pressure work to elucidate the effect of common fabrication procedures, relevant to solid-state battery applications. For example, variable-pressure impedance spectroscopy can elucidate the atomistic ion-conduction mechanisms through determination of activation volumes and can lead to identification of processing side-effects, allowing in turn the unlocking of the performance of solid electrolytes, as we have demonstrated here for Na_3PS_4.

CONCLUSION

We have enhanced our current understanding of the effect of mechanochemistry on the structural and ion transport properties of Na_3PS_4 through the combined use of diffraction (Bragg and PDF), spectroscopic (impedance, Raman, INS, and NMR), and ab initio simulations. We find that ball-milling imparts micro- and macrostrain on the material. The local tetragonal structural motif remains unchanged, but the average structure is pseudocubic, with disorder introduced in the Na-ion distribution. The stabilization of the cubic polymorph can be understood as a pressure-induced phase transition. Three parallel effects of the mechanochemical synthesis on ion transport at multiple scales are identified:

(i) Due to the mechanical pressure that acts on the solid electrolyte during the harsh mechanochemical conditions, significant strain is imparted on the material; this strain increases the activation volume, hindering ion transport.

(ii) The repeated impacts during the mechanochemical synthesis decrease the particle size of the resulting powder, facilitating its consolidation into highly ion-conducting pellets.

(iii) Mobile sodium defects are introduced into the Na_3PS_4 structure, enhancing ion transport.

While effect (i) hinders ion transport, effects (ii) and (iii) enhance it significantly, leading to an overall increase in ionic conductivity. Indeed, we show that the effect of ball-milling on increasing the ionic conductivity of Na_3PS_4 to $\sim 10^{-4}$ S/cm can be reproduced by applying external pressure on a sample from conventional high temperature synthesis. We conclude that the rational application of pressure is the key factor in exploiting the high ionic conductivity of Na_3PS_4. This can be achieved through either (a) mechanochemical synthesis, (b) application of high pressure (~ 1 GPa) during pellet (or device) fabrication, or (c) application of a moderate pressure of $\sim 100-250$ MPa during measurement (or device operation).

These results are of importance to the battery community, in which the effects of pressure and (micro)mechanics on performance have not been fully explored. Indeed, this study aims to inspire further work using variable-pressure diffraction and variable-pressure impedance spectroscopy on solid electrolyte materials.

METHODS

Synthesis. Three samples were considered in this work, following the work of Krauskopf et al.[7] and denoted in the same way. The reagents used were the binaries Na_2S and P_2S_5 (Sigma-Aldrich) utilized as received.

HT-tetragonal Na_3PS_4 was synthesized by a solid-state synthesis route as first reported by Jansen and Henseler.[1] Stoichiometric ratios of the reagents were intimately mixed first in a mortar pestle and then in a ball-mill jar (typically 5 g of precursors with 25 10 mm ZrO_2 balls in an 80 mL ZrO_2 jar, milled for 12 h at 500 rpm). The resulting powder was pelletized and placed in carbon-coated quartz tubes. The carbon-coating of the tubes was achieved by acetone pyrolysis and subsequent annealing at 1000 °C for 12 h under Ar. The quartz tubes were then flame-sealed under vacuum ($\sim 10^{-2}$ mbar) and placed in a furnace for reaction. The temperature of the furnace was slowly increased to 500 °C at 1 °C/min, held for 20 h, and naturally cooled to room temperature.

BM-cubic Na_3PS_4 was synthesized by a mechanochemical route as first reported by Hayashi et al.[4] Stoichiometric ratios of the reagents were intimately mixed in a mortar and pestle and placed in an 80 mL ZrO_2 ball-milling jar along with 60 g of 3 mm ZrO_2 balls. The jars were placed in a planetary ball-mill (Pulverisette 7 Premium, Fritsch) and milled for 12 h at 500 rpm (144 cycles of 5 min of milling followed by 15 min breaks to dissipate heat). After the milling treatment, the resulting powder was subjected to a heat treatment at 260 °C under vacuum in a vacuum oven (Büchi).

BM-tetragonal Na_3PS_4 was synthesized by a combination of the above methods as first reported by Krauskopf et al.:[7] a BM-cubic sample was pelletized and sealed in a quartz tube and then placed in an oven preheated to 500 °C for 20 min for a rapid thermal annealing.

In all cases, the products after synthesis were milled by pestle and mortar into fine powders for further analysis. All handling was performed in Ar-filled gloveboxes.

Bragg Diffraction. X-ray powder diffraction experiments were performed at the MSPD beamline[72,73] of the ALBA synchrotron in Barcelona, Spain. Samples were flame-sealed under Ar in 1 mm

diameter quartz capillaries. Diffractograms were collected at room temperature, in transmission geometry, using a position-sensitive MYTHEN detector and a wavelength of 0.8262 Å, selected using a Si 111 reflection double crystal monochromator. A well-crystallized $Na_2Ca_3Al_2F_{14}$ powder was also measured as the standard to extract the instrument resolution and allow for the quantitative analysis of the peak broadening in the Na_3PS_4 samples.

Neutron powder diffraction experiments were performed at the D2B beamline of the Institut Laue-Langevin (ILL) in Grenoble, France. Samples (~2 g) were sealed in cylindrical vanadium containers using indium wire. Diffractograms were collected at room temperature, in transmission geometry, using 128 ^{3}He counting tubes and a wavelength of 1.594 Å selected using the (335) reflection of Ge[115] monochromators.

The analysis of the Bragg diffraction data was performed using the programs in the Fullprof software suite.[74] The background was described as a linear interpolation between manually selected points. Le Bail fits were performed to describe the sample broadening using the Thompson−Cox−Hastings pseudo-Voigt function[75] (convoluted with the instrumental resolution in the case of X-rays). The apparent crystallite size and apparent microstrain were extracted from the X-ray data sets in accordance with the Scherrer−[76] and Stokes−Wilson[77] relations, respectively, as implemented in Fullprof.[74] In subsequent Rietveld analyses, occupancies were fixed to the Na_3PS_4 stoichiometry, and atomic positions and displacement parameters were fitted.

Maximum entropy method (MEM) calculations were performed using Dysnomia.[78] Structure visualizations were produced using VESTA.[79]

Pair Distribution Function Analysis. X-ray powder total scattering diffraction experiments were performed at the 11-ID-B beamline of the Advanced Photon Source at Argonne National Laboratory using high-energy X-rays (λ = 0.2113 Å) for high values of momentum transfer (Q = 24.5 Å^{-1}). Samples were flame-sealed under Ar in quartz capillaries. One dimensional diffraction data were obtained by integrating the raw 2D total scattering data in Fit2D. Pair distribution functions (PDFs) were extracted from the background- and Compton scattering-corrected data following Fourier transform using PDFgetX2.[80]

The analysis of the PDFs was performed using the PDFfit2 engine as implemented in PDFgui.[80] Structural refinements were limited to single-unit-cells (no supercells) and constrained by the space group symmetry observed in Bragg diffraction ($P\overline{4}2_1c$ or $I\overline{4}3m$). In agreement with the observation of Krauskopf et al.,[7] the range 1.5−4 Å in the PDFs, which corresponds to the first neighbors P−S, Na−S, and S−S, cannot be well-described with the same peak shape as the remaining PDF and was omitted from the refinements. This is probably related to the strong covalent character of the PS_4^{3-} moiety, in contrast with the ionic interactions at higher r. The following parameters were refined in this order: (1) scale factor, (2) lattice parameters, (3) atomic positions, and (4) thermal displacement parameters. For fits of the whole PDF (4−70 Å), the instrumental resolution parameters Q_{damp} and Q_{broad} were also refined individually at the end of the refinement process.

The quality of each refinement is quantified by the reliability factor weighted R-value, R_w, which describes the difference between the experimental data (obs) and the fit (calc) of each data point:

$$R_w = \sqrt{\frac{\sum_{i=1}^{N} w(r_i)[G_{obs}(r_i) - G_{calc}(r_i)]^2}{\sum_{i=1}^{N} w(r_i) G_{obs}^2(r_i)}}$$

with G_{obs} and G_{calc} being the observed and calculated PDF and $w(r_i)$ the weight for each data point.

NMR Spectroscopy. ^{23}Na and ^{31}P MAS NMR spectra were acquired on a Bruker 500 MHz (11.8 T) magnet with the Avance III console using a Bruker 2.5 mm HFX MAS probe, a regular zg/one-pulse pulse program with π/2 and π/4 pulses for ^{31}P and ^{23}Na, respectively, and a MAS frequency of 25 kHz. The spectra were externally referenced against solid NaCl (7.21 ppm)[81] for ^{23}Na and $NH_4H_2PO_4$ powder (0.8 ppm) for ^{31}P. The reference compounds

were used for pulse length optimization as well. TopSpin software was used for raw data handling, and spectra were fitted using dmfit software[82] and the Q mas 1/2 model.

Raman Spectroscopy. The samples used for Raman spectroscopy were prepared identically to the X-ray diffraction samples, i.e., flame-sealed under Ar in 1 mm diameter quartz capillaries. Spectra were measured using a Renishaw inVia Qontor confocal microscope equipped with a 532 nm laser excitation source. Spectra were collected in backscattering geometry using a Centrus detector in the range 15−1280 cm^{-1}. Typically, three spectra were recorded and added for a total acquisition time of 3 × 60 = 180 s. The incident power of the laser was set to 5 mW focused by a 10× objective to a spot of about 10 μm on the sample. These parameters were optimized to maximize the signal−over−noise ratio while avoiding excessive local heating and decomposition of the sample made evident by distortion of the spectra.

Inelastic Neutron Scattering. Samples (~2 g) for inelastic neutron scattering (INS) measurements were lightly compacted into pellets and sealed in 10 mm diameter SiO_2 ampules under vacuum (~10^{-2} mbar). The ampules were placed in custom-made Nb holders and subsequently in an evacuated furnace environment. Spectra were measured at room temperature using the cold-neutron, time-of-flight, time-focusing, IN6 spectrometer at the Institut Laue-Langevin (ILL) in Grenoble, France. An incident wavelength of 5.12 Å was used, offering an elastic energy resolution of ~0.1 meV, as determined from a standard vanadium sample. The vanadium sample was also used to calibrate the detectors. The measurements were carried out in the high-resolution, inelastic time focusing mode. The spectra were collected in the up-scattering, neutron energy-gain mode up to 80 meV in terms of the generalized density of states (GDOS). We note that, in contrast to the vibrational density of states, the INS-measured GDOS involves a weighting of the scatterers (ions) with their scattering powers. Data reduction and treatment, including detector efficiency calibration and background subtraction, were performed using standard ILL tools. Data reduction included measuring an identical empty SiO_2 ampule and Nb container under the same experimental conditions. In the incoherent approximation,[83] the Q-averaged, one-phonon[84] GDOS, $g^{(n)}(E)$, is related to the measured dynamical structure factor, $S(Q, E)$, from INS by

$$g^{(n)}(E) = A \left\langle \frac{e^{2W(Q)}}{Q^2} \frac{E}{n(E, T) + \frac{1}{2} \pm \frac{1}{2}} S(Q, E) \right\rangle$$

where A is a normalization constant, $2W(Q)$ is the Debye−Waller factor, and $n(E, T)$ is the thermal occupation factor (Bose-factor correction) equal to $[\exp(E/k_BT) - 1]^{-1}$. The + or − signs correspond to neutron energy loss or gain, respectively, and the brackets indicate an average over all Q.

Vibrational Spectra Calculations. The vibrational spectra of Na_3PS_4 were simulated using density functional theory (DFT) as implemented in the all-electron code CRYSTAL17,[85] where the crystalline wave function is expanded as a linear combination of atomic orbitals and further expanded by a consistent triple-ζ plus polarization basis-set.[86,87] The total energy during the geometry relaxation and later in the phonon calculations was converged within ~3.0 × 10^{-9} eV and integrated over a well-converged and symmetrized 8 × 8 × 8 k-point mesh (i.e., the shrinking factor is 8). The unknown exchange-correlation contribution to the total energy was approximated by the range-separated hybrid functional proposed by Heyd−Scuseria−Ernzerhof HSE06.[88,89] The truncation of the (infinite) Coulomb and exchange series was set by the tolerances (TOLINTEG), 10^{-7}, 10^{-7}, 10^{-7}, 10^{-9}, and 10^{-30}, while an XXLGRID was used for the integration of the charge density. Raman frequencies of the two polymorphs were computed at the Γ-point only, employing the finite difference method. Thus, the dynamical matrix was developed using a step size of 0.003 Å for each displacement.

Geometry Optimization Calculations. Ab initio geometry optimization calculations in this work were carried out using DFT

with the Vienna ab initio simulation package (VASP).[90] Plane-wave cutoff energies of 520 eV were utilized for the geometry optimization calculations. The projector augmented wave method[91] and the PBEsol exchange-correlation functional[92] were employed for all calculations. A k-point mesh spacing smaller than 0.05 Å^{-1} was used for the geometry optimization calculations.

Impedance Spectroscopy. Measurements in temperature were performed on pelletized samples with carbon electrodes. The synthesized Na$_3$PS$_4$ powders were placed between two 6 mm diameter graphite paper electrodes (Papyex, Mersen) dried overnight under vacuum at 200 °C. The carbon–Na$_3$PS$_4$–carbon composite pellets were pressed using a 6 mm diameter steel mold and hydraulic press. The pressure was slowly increased in increments of 0.5 tons up to 2 tons (corresponding to ~700 MPa). In all cases, this resulted in highly dense pellets of >95% compacity with respect to the crystallographic density (2.1 g/cm^3). The composite pellets were mounted on a CESH sample holder (Bio-Logic) and placed in an ITS system (Bio-Logic) allowing temperature control in the range from −15 to 100 °C. The spectra were collected by applying an AC excitation voltage of 50 mV from 10 Hz to 30 MHz using an MTZ-35 impedance analyzer (Bio-Logic).

Measurements in pressure were performed on similar samples pressed in custom-made 10 mm diameter polycarbonate molds and steel pistons. The samples were pressed in an Ar-filled glovebox up to 5 tons (~625 MPa) and protected from air exposure using vacuum grease on the pistons. Typically, ~100 mg of Na$_3$PS$_4$ powder was used giving rise to an electrolyte thickness of ~0.6 mm. The ensemble was removed from the glovebox, and measurements were performed "in situ" using the steel pistons as electrodes while varying the applied uniaxial pressure and the same impedance parameters as above. Electrical tape was used to insulate the piston-electrodes from the hydraulic press.

The analysis of the impedance spectra was performed using the RELAXIS3 (rhd instruments) and ZView (Scribner) softwares.

■ ASSOCIATED CONTENT

Ⓢ Supporting Information

The Supporting Information is available free of charge at https://pubs.acs.org/doi/10.1021/jacs.0c06668.

> Rietveld refinements of Bragg diffractograms, discussion of Rietveld fit quality, group–subgroup relationship between α- and β-Na$_3$PS$_4$, Williamson–Hall plot, comparison of the X-ray PDFs, refinements of the full X-ray PDFs, fitting of calculated pressure–volume–energy data, summary of fits of the diffractograms of BM-cub-Na$_3$PS$_4$, additional solid-state NMR experimental details, derivation of the activation volume formula, literature data on the compressibility of Na$_3$PS$_4$, determination of activation volume of Na$_3$PS$_4$, fitted capacitances of Na$_3$PS$_4$ from variable-pressure impedance spectra, determination of activation volume of Na$_3$SbS$_4$, transmission electron microscopy, chronological evolution of conductivity in HT-tet-Na$_3$PS$_4$ under pressure, and assumptions and limitations of the variable-pressure impedance spectroscopy setup (PDF)

■ AUTHOR INFORMATION

Corresponding Authors

Theodosios Famprikis − *Laboratoire de Réactivité et Chimie des Solides (LRCS), CNRS UMR 7314, Université de Picardie Jules Verne, 80039 Amiens, France; Department of Chemistry, University of Bath, Bath BA2 7AY, United Kingdom; ALISTORE European Research Institute, CNRS FR 3104, 80039 Amiens, France; Réseau sur le Stockage Électrochimique de l'Énergie (RS2E), CNRS FR 3459, 80039 Amiens, France;* orcid.org/0000-0002-7946-1445; Email: theo.famprikis@u-picardie.fr

M. Saiful Islam − *Department of Chemistry, University of Bath, Bath BA2 7AY, United Kingdom; ALISTORE European Research Institute, CNRS FR 3104, 80039 Amiens, France;* orcid.org/0000-0003-3882-0285; Email: m.s.islam@bath.ac.uk

Christian Masquelier − *Laboratoire de Réactivité et Chimie des Solides (LRCS), CNRS UMR 7314, Université de Picardie Jules Verne, 80039 Amiens, France; ALISTORE European Research Institute, CNRS FR 3104, 80039 Amiens, France; Réseau sur le Stockage Électrochimique de l'Énergie (RS2E), CNRS FR 3459, 80039 Amiens, France;* orcid.org/0000-0001-7289-1015; Email: christian.masquelier@u-picardie.fr

Authors

Ö. Ulaş Kudu − *Laboratoire de Réactivité et Chimie des Solides (LRCS), CNRS UMR 7314, Université de Picardie Jules Verne, 80039 Amiens, France*

James A. Dawson − *Department of Chemistry, University of Bath, Bath BA2 7AY, United Kingdom; Chemistry—School of Natural and Environmental Sciences, Newcastle University, Newcastle upon Tyne NE1 7RU, United Kingdom;* orcid.org/0000-0002-3946-5337

Pieremanuele Canepa − *Department of Materials Science and Engineering, The National University of Singapore, 117576, Singapore;* orcid.org/0000-0002-5168-9253

François Fauth − *CELLS—ALBA Synchrotron, Cerdanyola del Vallès, 08290 Barcelona, Spain;* orcid.org/0000-0001-9465-3106

Emmanuelle Suard − *Institut Laue-Langevin (ILL), 38042 Grenoble, France;* orcid.org/0000-0001-5966-5929

Mohamed Zbiri − *Institut Laue-Langevin (ILL), 38042 Grenoble, France;* orcid.org/0000-0002-0413-0262

Damien Dambournet − *Physico-Chimie des Electrolytes et Nano-systèmes Interfaciaux (PHENIX), CNRS UMR 8234, Sorbonne Université, F-75005 Paris, France; Réseau sur le Stockage Électrochimique de l'Énergie (RS2E), CNRS FR 3459, 80039 Amiens, France*

Olaf J. Borkiewicz − *X-ray Science Division, Advanced Photon Source, Argonne National Laboratory, Argonne, Illinois 60439, United States*

Houssny Bouyanfif − *Laboratoire de Physique de la Matière Condensée (LPMC), UR 2081, Université de Picardie Jules Verne, Amiens 80039, France*

Steffen P. Emge − *Department of Chemistry, University of Cambridge, Cambridge CB2 1EW, United Kingdom;* orcid.org/0000-0001-8613-9465

Sorina Cretu − *Laboratoire de Réactivité et Chimie des Solides (LRCS), CNRS UMR 7314, Université de Picardie Jules Verne, 80039 Amiens, France;* orcid.org/0000-0001-9358-7768

Jean-Noël Chotard − *Laboratoire de Réactivité et Chimie des Solides (LRCS), CNRS UMR 7314, Université de Picardie Jules Verne, 80039 Amiens, France;* orcid.org/0000-0002-9867-7954

Clare P. Grey − *Department of Chemistry, University of Cambridge, Cambridge CB2 1EW, United Kingdom; ALISTORE European Research Institute, CNRS FR 3104, 80039 Amiens, France;* orcid.org/0000-0001-5572-192X

Wolfgang G. Zeier − *Institute of Inorganic and Analytical Chemistry, University of Muenster, 48149 Muenster, Germany;* orcid.org/0000-0001-7749-5089

Complete contact information is available at:

Author Contributions

T.F. coordinated the work, performed synthesis, neutron diffraction, Raman- and impedance spectroscopy experiments, as well as the global data analysis and composed the manuscript. J.A.D. performed the geometry optimization calculations as a function of pressure. P.C. performed the calculations of the vibrational spectra. F.F. performed the x-ray Bragg diffraction experiments. E.S. assisted with the neutron Bragg diffraction experiments. M.Z. performed the INS experiments and associated analysis. O.J.B. performed x ray total scattering experiments and D.D. assisted with the associated analysis. H.B. assisted with Raman experiments and their interpretation. S.P.E. performed NMR experiments and C.P.G. assisted with the associated analysis and interpretation. S.C. performed TEM experiments. J.-N.C. assisted with the analysis of Bragg data. U.K. and W.G.Z. provided in depth comments on the manuscript. M.S.I. and C.M. supervised the work. The final manuscript includes contributions from authors.

Notes

The authors declare no competing financial interest.

■ REFERENCES

(1) Jansen, M.; Henseler, U. Synthesis, Structure Determination, and Ionic Conductivity of Sodium Tetrathiophosphate. *J. Solid State Chem.* **1992**, *99* (1), 110−119.

(2) Famprikis, T.; Dawson, J. A.; Fauth, F.; Clemens, O.; Suard, E.; Fleutot, B.; Courty, M.; Chotard, J.-N.; Islam, M. S.; Masquelier, C. A New Superionic Plastic Polymorph of the Na⁺ Conductor Na₃PS₄. *ACS Mater. Lett.* **2019**, *1* (6), 641−646.

(3) Famprikis, T.; Canepa, P.; Dawson, J. A.; Islam, M. S.; Masquelier, C. Fundamentals of Inorganic Solid-State Electrolytes for Batteries. *Nat. Mater.* **2019**, *18* (12), 1278−1291.

(4) Hayashi, A.; Noi, K.; Sakuda, A.; Tatsumisago, M. Superionic Glass-Ceramic Electrolytes for Room-Temperature Rechargeable Sodium Batteries. *Nat. Commun.* **2012**, *3* (1), 856.

(5) Hayashi, A.; Noi, K.; Tanibata, N.; Nagao, M.; Tatsumisago, M. High Sodium Ion Conductivity of Glass-Ceramic Electrolytes with Cubic Na₃PS₄. *J. Power Sources* **2014**, *258*, 420−423.

(6) Noi, K.; Hayashi, A.; Tatsumisago, M. Structure and Properties of the Na₂S-P₂S₅ Glasses and Glass-Ceramics Prepared by Mechanical Milling. *J. Power Sources* **2014**, *269*, 260−265.

(7) Krauskopf, T.; Culver, S. P.; Zeier, W. G. Local Tetragonal Structure of the Cubic Superionic Conductor Na₃PS₄. *Inorg. Chem.* **2018**, *57* (8), 4739−4744.

(8) Nishimura, S.; Tanibata, N.; Hayashi, A.; Tatsumisago, M.; Yamada, A. The Crystal Structure and Sodium Disorder of High-Temperature Polymorph β-Na₃PS₄. *J. Mater. Chem. A* **2017**, *5* (47), 25025−25030.

(9) Tanibata, N.; Noi, K.; Hayashi, A.; Kitamura, N.; Idemoto, Y.; Tatsumisago, M. X-Ray Crystal Structure Analysis of Sodium-Ion Conductivity in 94 Na₃PS₄·6 Na₄SiS₄ Glass-Ceramic Electrolytes. *ChemElectroChem* **2014**, *1* (7), 1130−1132.

(10) Palatnik, L. S.; Kosevich, V. M.; Tyrina, L. V. Electron Diffraction Examination of the Metastable Phases in the Alloys Au-Sb, In- Sb, In- Bi, and In- Bi- Sb. *Russ. Phys. Met. Met.* **1961**, *11* (2), 75−80.

(11) Yu, C.; Ganapathy, S.; de Klerk, N. J. J.; van Eck, E. R. H.; Wagemaker, M. Na-Ion Dynamics in Tetragonal and Cubic Na₃PS₄, a Na-Ion Conductor for Solid State Na-Ion Batteries. *J. Mater. Chem. A* **2016**, *4* (39), 15095−15105.

(12) Bo, S.-H.; Wang, Y.; Ceder, G. Structural and Na-Ion Conduction Characteristics of Na₃PSₓSe₄₋ₓ. *J. Mater. Chem. A* **2016**, *4* (23), 9044−9053.

(13) De Klerk, N. J. J.; Wagemaker, M. Diffusion Mechanism of the Sodium-Ion Solid Electrolyte Na₃PS₄ and Potential Improvements of Halogen Doping. *Chem. Mater.* **2016**, *28* (9), 3122−3130.

(14) Hayashi, A.; Tatsumisago, M. *All-Solid-State Secondary Cell.* US 20170222259 A1.

(15) Takeuchi, S.; Suzuki, K.; Hirayama, M.; Kanno, R. Sodium Superionic Conduction in Tetragonal Na₃PS₄. *J. Solid State Chem.* **2018**, *265*, 353−358.

(16) Nguyen, H.; Banerjee, A.; Wang, X.; Tan, D.; Wu, E. A.; Doux, J.-M.; Stephens, R.; Verbist, G.; Meng, Y. S. Single-Step Synthesis of Highly Conductive Na₃PS₄ Solid Electrolyte for Sodium All Solid-State Batteries. *J. Power Sources* **2019**, *435* (April), 126623.

(17) Kudu, Ö. U.; Famprikis, T.; Fleutot, B.; Braida, M.-D.; Le Mercier, T.; Islam, M. S.; Masquelier, C. A Review of Structural Properties and Synthesis Methods of Solid Electrolyte Materials in the Li₂S-P₂S₅ Binary System. *J. Power Sources* **2018**, *407*, 31−43.

(18) Breuer, S.; Uitz, M.; Wilkening, H. M. R. Rapid Li Ion Dynamics in the Interfacial Regions of Nanocrystalline Solids. *J. Phys. Chem. Lett.* **2018**, *9* (8), 2093−2097.

(19) Qiao, A.; Tao, H.; Yue, Y. Enhancing Ionic Conductivity in Ag₃PS₄ via Mechanical Amorphization. *J. Non-Cryst. Solids* **2019**, *521* (April), 119476.

(20) Rao, R. P.; Zhang, X.; Phuah, K. C.; Adams, S. Mechanochemical Synthesis of Fast Sodium Ion Conductor Na₁₁Sn₂PSe₁₂ Enables First Sodium-Selenium All-Solid-State Battery. *J. Mater. Chem. A* **2019**, *7* (36), 20790−20798.

(21) Schlem, R.; Muy, S.; Prinz, N.; Banik, A.; Shao-Horn, Y.; Zobel, M.; Zeier, W. G. Mechanochemical Synthesis: A Tool to Tune Cation Site Disorder and Ionic Transport Properties of Li₃MCl₆ (M = Y, Er) Superionic Conductors. *Adv. Energy Mater.* **2020**, *10* (6), 1903719.

(22) Liu, Z.; Fu, W.; Payzant, E. A.; Yu, X.; Wu, Z.; Dudney, N. J.; Kiggans, J.; Hong, K.; Rondinone, A. J.; Liang, C. Anomalous High Ionic Conductivity of Nanoporous β-Li₃PS₄. *J. Am. Chem. Soc.* **2013**, *135* (3), 975−978.

(23) Tsukasaki, H.; Mori, S.; Morimoto, H.; Hayashi, A.; Tatsumisago, M. Direct Observation of a Non-Crystalline State of Li₂S-P₂S₅ Solid Electrolytes. *Sci. Rep.* **2017**, *7* (1), 4142.

(24) Fuchs, T.; Culver, S. P.; Till, P.; Zeier, W. G. Defect-Mediated Conductivity Enhancements in $Na_{3-x}Pn_{1-x}W_xS_4$ (Pn = P, Sb) Using Aliovalent Substitutions. *ACS Energy Lett.* **2020**, *5* (1), 146−151.

(25) Hayashi, A.; Masuzawa, N.; Yubuchi, S.; Tsuji, F.; Hotehama, C.; Sakuda, A.; Tatsumisago, M. A Sodium-Ion Sulfide Solid Electrolyte with Unprecedented Conductivity at Room Temperature. *Nat. Commun.* **2019**, *10* (1), 5266.

(26) Feng, X.; Chien, P.-H.; Zhu, Z.; Chu, I.-H.; Wang, P.; Immediato-Scuotto, M.; Arabzadeh, H.; Ong, S. P.; Hu, Y.-Y. Studies of Functional Defects for Fast Na-Ion Conduction in $Na_{3-y}PS_{4-x}Cl_x$ with a Combined Experimental and Computational Approach. *Adv. Funct. Mater.* **2019**, *29* (9), 1807951.

(27) Moon, C. K.; Lee, H.-J.; Park, K. H.; Kwak, H.; Heo, J. W.; Choi, K.; Yang, H.; Kim, M.-S.; Hong, S.-T.; Lee, J. H.; Jung, Y. S. Vacancy-Driven Na^+ Superionic Conduction in New Ca-Doped Na_3PS_4 for All-Solid-State Na-Ion Batteries. *ACS Energy Lett.* **2018**, *3* (10), 2504−2512.

(28) Chu, I.-H.; Kompella, C. S.; Nguyen, H.; Zhu, Z.; Hy, S.; Deng, Z.; Meng, Y. S.; Ong, S. P. Room-Temperature All-Solid-State Rechargeable Sodium-Ion Batteries with a Cl-Doped Na_3PS_4 Superionic Conductor. *Sci. Rep.* **2016**, *6* (1), 33733.

(29) Zhu, Z.; Chu, I.-H.; Deng, Z.; Ong, S. P. Role of Na^+ Interstitials and Dopants in Enhancing the Na^+ Conductivity of the Cubic Na_3PS_4 Superionic Conductor. *Chem. Mater.* **2015**, *27* (24), 8318−8325.

(30) Tanibata, N.; Noi, K.; Hayashi, A.; Tatsumisago, M. Preparation and Characterization of Highly Sodium Ion Conducting Na_3PS_4-Na_4SiS_4 Solid Electrolytes. *RSC Adv.* **2014**, *4* (33), 17120−17123.

(31) Dawson, J. A.; Canepa, P.; Clarke, M. J.; Famprikis, T.; Ghosh, D.; Islam, M. S. Toward Understanding the Different Influences of Grain Boundaries on Ion Transport in Sulfide and Oxide Solid Electrolytes. *Chem. Mater.* **2019**, *31* (14), 5296−5304.

(32) Burmeister, C. F.; Kwade, A. Process Engineering with Planetary Ball Mills. *Chem. Soc. Rev.* **2013**, *42* (18), 7660.

(33) Seidel, S.; Zeier, W. G.; Pöttgen, R. The Polymorphs of the Na^+ Ion Conductor Na_3PS_4 Viewed from the Perspective of a Group-Subgroup Scheme. *Z. Kristallogr. - Cryst. Mater.* **2020**, *235* (1−2), 1−6.

(34) Krauskopf, T.; Pompe, C.; Kraft, M. A.; Zeier, W. G. Influence of Lattice Dynamics on Na^+ Transport in the Solid Electrolyte $Na_3PS_{4-x}Se_x$. *Chem. Mater.* **2017**, *29* (20), 8859−8869.

(35) Tanibata, N.; Deguchi, M.; Hayashi, A.; Tatsumisago, M. All-Solid-State Na/S Batteries with a Na_3PS_4 Electrolyte Operating at Room Temperature. *Chem. Mater.* **2017**, *29* (12), 5232−5238.

(36) Eckert, H.; Zhang, Z.; Kennedy, J. H. Structural Transformation of Non-Oxide Chalcogenide Glasses. The Short-Range Order of Li_2S-P_2S_5 Glasses Studied by Quantitative ^{31}P and $^{6,7}Li$ High-Resolution Solid-State NMR. *Chem. Mater.* **1990**, *2* (3), 273−279.

(37) Dietrich, C.; Weber, D. A.; Sedlmaier, S. J.; Indris, S.; Culver, S. P.; Walter, D.; Janek, J.; Zeier, W. G. Lithium Ion Conductivity in Li_2S-P_2S_5 Glasses - Building Units and Local Structure Evolution during the Crystallization of Superionic Conductors Li_3PS_4, $Li_7P_3S_{11}$ and $Li_4P_2S_7$. *J. Mater. Chem. A* **2017**, *5* (34), 18111−18119.

(38) Zhang, W.; Schröder, D.; Arlt, T.; Manke, I.; Koerver, R.; Pinedo, R.; Weber, D. A.; Sann, J.; Zeier, W. G.; Janek, J. (Electro)Chemical Expansion during Cycling: Monitoring the Pressure Changes in Operating Solid-State Lithium Batteries. *J. Mater. Chem. A* **2017**, *5* (20), 9929−9936.

(39) Wu, X.; El Kazzi, M.; Villevieille, C. Surface and Morphological Investigation of the Electrode/Electrolyte Properties in an All-Solid-State Battery Using a Li_2S-P_2S_5 Solid Electrolyte. *J. Electroceram.* **2017**, *38* (2−4), 207−214.

(40) Doux, J.-M.; Nguyen, H.; Tan, D. H. S.; Banerjee, A.; Wang, X.; Wu, E. A.; Jo, C.; Yang, H.; Meng, Y. S. Stack Pressure Considerations for Room-Temperature All-Solid-State Lithium Metal Batteries. *Adv. Energy Mater.* **2020**, *10*, 1903253.

(41) Doux, J.-M.; Yang, Y.; Tan, D. H. S.; Nguyen, H.; Wu, E. A.; Wang, X.; Banerjee, A.; Meng, Y. S. Pressure Effects on Sulfide Electrolytes for All Solid-State Batteries. *J. Mater. Chem. A* **2020**, *8*, 5049−5055.

(42) Hoshino, H.; Shimoji, M. The Effect of the Hydrostatic Pressure on the Electrical Conductivity of Silver Iodide. *J. Phys. Chem. Solids* **1972**, *33* (12), 2303−2309.

(43) Hoshino, H.; Yanagiya, H.; Shimoji, M. Effect of Hydrostatic Pressure on the Electrical Conductivity of Ag_3SBr and β-Ag_3SI. *J. Chem. Soc., Faraday Trans. 1* **1974**, *70*, 281.

(44) Kim, K. S.; Paik, W.-K. Effects of Temperature and Pressure on Conductance of Solid Electrolyte, $RbAg_4I_5$. *J. Chem. Eng. Data* **1975**, *20* (4), 356−359.

(45) Wagener, K. Die Druckabhängigkeit Der Ionenleitfähigkeit Anomaler Mischkristalle von AgBr Und AgJ. *Z. Phys. Chem.* **1960**, *23* (5-6), 305−312.

(46) Radzilowski, R. H.; Kummer, J. T. The Hydrostatic Pressure Dependence of the Ionic Conductivity of β-Aluminas. *J. Electrochem. Soc.* **1971**, *118* (5), 714.

(47) Itoh, K.; Kondo, K.; Sawaoka, A.; Saito, S. Effect of Pressure on the Ionic Conduction of Na-β-Alumina. *Jpn. J. Appl. Phys.* **1975**, *14* (8), 1237−1238.

(48) Mezaki, T.; Kuronuma, Y.; Oikawa, I.; Kamegawa, A.; Takamura, H. Li-Ion Conductivity and Phase Stability of Ca-Doped $LiBH_4$ under High Pressure. *Inorg. Chem.* **2016**, *55* (20), 10484−10489.

(49) Inaguma, Y.; Yu, J.; Shan, Y. J.; Itoh, M.; Nakamura, T. The Effect of the Hydrostatic Pressure on the Ionic Conductivity in a Perovskite Lanthanum Lithium Titanate. *J. Electrochem. Soc.* **1995**, *142* (1), 142−145.

(50) Mellander, B.-E.; Lazarus, D. Electrical Conductivity and Activation Volume for α-Li_2SO_4. *Phys. Rev. B: Condens. Matter Mater. Phys.* **1985**, *31* (10), 6801−6803.

(51) Bose, D. N.; Parthasarathy, G.; Mazumdar, D.; Gopal, E. S. R. Resistivity Maxima in Lithium Fast-Ion Conductors at High Pressure. *Phys. Rev. Lett.* **1984**, *53* (14), 1368−1371.

(52) Kafalas, J. A.; Cava, R. J. Abstract. In *Fast Ion Transport in Solids*; Vashishta, P., Mundy, J. N., Shenoy, G. K., Eds.; Elsevier: Amsterdam, 1979; p 149.

(53) Wang, H.; Yu, M.; Wang, Y.; Feng, Z.; Wang, Y.; Lü, X.; Zhu, J.; Ren, Y.; Liang, C. In-Situ Investigation of Pressure Effect on Structural Evolution and Conductivity of Na_3SbS_4 Superionic Conductor. *J. Power Sources* **2018**, *401* (April), 111−116.

(54) Fontanella, J. J. Pressure and Temperature Variation of the Electrical Conductivity of Poly(Propylene Glycol) Containing $LiCF_3SO_3$. *J. Chem. Phys.* **1999**, *111* (15), 7103−7109.

(55) Brug, G. J.; van den Eeden, A. L. G.; Sluyters-Rehbach, M.; Sluyters, J. H. The Analysis of Electrode Impedances Complicated by the Presence of a Constant Phase Element. *J. Electroanal. Chem. Interfacial Electrochem.* **1984**, *176* (1−2), 275−295.

(56) Deng, Z.; Wang, Z.; Chu, I.-H.; Luo, J.; Ong, S. P. Elastic Properties of Alkali Superionic Conductor Electrolytes from First Principles Calculations. *J. Electrochem. Soc.* **2016**, *163* (2), A67−A74.

(57) Nose, M.; Kato, A.; Sakuda, A.; Hayashi, A.; Tatsumisago, M. Evaluation of Mechanical Properties of Na_2S-P_2S_5 Sulfide Glass Electrolytes. *J. Mater. Chem. A* **2015**, *3* (44), 22061−22065.

(58) Liu, W.; Sun, H.; Niu, Y. Theoretical Investigation the Mechanical and Thermodynamic Properties of α and β-Phase Solid Electrolytes Na_3PS_4. *J. Electrochem. Soc.* **2019**, *166* (13), A3011−A3018.

(59) Yu, Z.; Shang, S.-L.; Seo, J.-H.; Wang, D.; Luo, X.; Huang, Q.; Chen, S.; Lu, J.; Li, X.; Liu, Z.-K.; Wang, D. Exceptionally High Ionic Conductivity in $Na_3P_{0.62}As_{0.38}S_4$ with Improved Moisture Stability for Solid-State Sodium-Ion Batteries. *Adv. Mater.* **2017**, *29* (16), 1605561.

(60) Rush, L. E.; Hood, Z. D.; Holzwarth, N. A. W. Unraveling the Electrolyte Properties of Na_3SbS_4 through Computation and Experiment. *Phys. Rev. Mater.* **2017**, *1* (7), 075405.

(61) Shannon, R. D. Revised Effective Ionic Radii and Systematic Studies of Interatomic Distances in Halides and Chalcogenides. *Acta Crystallogr., Sect. A: Cryst. Phys., Diffr., Theor. Gen. Crystallogr.* **1976**, *32* (5), 751−767.

(62) Zhang, L.; Yang, K.; Mi, J.; Lu, L.; Zhao, L.; Wang, L.; Li, Y.; Zeng, H. Na_3PSe_4: A Novel Chalcogenide Solid Electrolyte with High Ionic Conductivity. *Adv. Energy Mater.* **2015**, *5* (24), 2−6.

(63) Wang, N.; Yang, K.; Zhang, L.; Yan, X.; Wang, L.; Xu, B. Improvement in Ion Transport in Na_3PSe_4-Na_3SbSe_4 by Sb Substitution. *J. Mater. Sci.* **2018**, *53* (3), 1987−1994.

(64) Krauskopf, T.; Muy, S.; Culver, S. P.; Ohno, S.; Delaire, O.; Shao-Horn, Y.; Zeier, W. G. Comparing the Descriptors for Investigating the Influence of Lattice Dynamics on Ionic Transport Using the Superionic Conductor $Na_3PS_{4-x}Se_x$. *J. Am. Chem. Soc.* **2018**, *140* (43), 14464−14473.

(65) Xiong, S.; Liu, Z.; Rong, H.; Wang, H.; McDaniel, M.; Chen, H. $Na_3SbSe_{4-x}S_x$ as Sodium Superionic Conductors. *Sci. Rep.* **2018**, *8* (1), 9146.

(66) Ohno, S.; Bernges, T.; Buchheim, J.; Duchardt, M.; Hatz, A.-K.; Kraft, M. A.; Kwak, H.; Santhosha, A. L.; Liu, Z.; Minafra, N.; Tsuji, F.; Sakuda, A.; Schlem, R.; Xiong, S.; Zhang, Z.; Adelhelm, P.; Chen, H.; Hayashi, A.; Jung, Y. S.; Lotsch, B. V.; Roling, B.; Vargas-Barbosa, N. M.; Zeier, W. G. How Certain Are the Reported Ionic Conductivities of Thiophosphate-Based Solid Electrolytes? An Interlaboratory Study. *ACS Energy Lett.* **2020**, *5* (3), 910−915.

(67) Garcia-Mendez, R.; Smith, J. G.; Neuefeind, J. C.; Siegel, D. J.; Sakamoto, J. Correlating Macro and Atomic Structure with Elastic Properties and Ionic Transport of Glassy Li_2S-P_2S_5 (LPS) Solid Electrolyte for Solid-State Li Metal Batteries. *Adv. Energy Mater.* **2020**, *10* (19), 2000335.

(68) Hayashi, A.; Masuzawa, N.; Yubuchi, S.; Tsuji, F.; Hotehama, C.; Sakuda, A.; Tatsumisago, M. A Sodium-Ion Sulfide Solid Electrolyte with Unprecedented Conductivity at Room Temperature. *Nat. Commun.* **2019**, *10* (1), 5266.

(69) Lunghammer, S.; Ma, Q.; Rettenwander, D.; Hanzu, I.; Tietz, F.; Wilkening, H. M. R. Bulk and Grain-Boundary Ionic Conductivity in Sodium Zirconophosphosilicate $Na_3Zr_2(SiO_4)_2PO_4$ (NASICON). *Chem. Phys. Lett.* **2018**, *701*, 147−150.

(70) Rettenwander, D.; Welzl, A.; Pristat, S.; Tietz, F.; Taibl, S.; Redhammer, G. J.; Fleig, J. A Microcontact Impedance Study on NASICON-Type $Li_{1+x}Al_xTi_{2-x}(PO_4)_3$ ($0 \leq x \leq 0.5$) Single Crystals. *J. Mater. Chem. A* **2016**, *4* (4), 1506−1513.

(71) Iwasaki, R.; Hori, S.; Kanno, R.; Yajima, T.; Hirai, D.; Kato, Y.; Hiroi, Z. Weak Anisotropic Lithium-Ion Conductivity in Single Crystals of $Li_{10}GeP_2S_{12}$. *Chem. Mater.* **2019**, *31* (10), 3694−3699.

(72) Fauth, F.; Peral, I.; Popescu, C.; Knapp, M. The New Material Science Powder Diffraction Beamline at ALBA Synchrotron. *Powder Diffr.* **2013**, *28* (S2), S360−S370.

(73) Fauth, F.; Boer, R.; Gil-Ortiz, F.; Popescu, C.; Vallcorba, O.; Peral, I.; Fullà, D.; Benach, J.; Juanhuix, J. The Crystallography Stations at the Alba Synchrotron. *Eur. Phys. J. Plus* **2015**, *130* (8), 160.

(74) Rodríguez-Carvajal, J.; Roisnel, T. Line Broadening Analysis Using FullProf*: Determination of Microstructural Properties. *Mater. Sci. Forum* **2004**, *443−444*, 123−126.

(75) Thompson, P.; Cox, D. E.; Hastings, J. B. Rietveld Refinement of Debye-Scherrer Synchrotron X-Ray Data from Al_2O_3. *J. Appl. Crystallogr.* **1987**, *20* (2), 79−83.

(76) Patterson, A. L. The Scherrer Formula for X-Ray Particle Size Determination. *Phys. Rev.* **1939**, *56* (10), 978−982.

(77) Stokes, A. R.; Wilson, A. J. C. The Diffraction of X Rays by Distorted Crystal Aggregates - I. *Proc. Phys. Soc.* **1944**, *56* (3), 174−181.

(78) Momma, K.; Ikeda, T.; Belik, A. A.; Izumi, F. Dysnomia, a Computer Program for Maximum-Entropy Method (MEM) Analysis and Its Performance in the MEM-Based Pattern Fitting. *Powder Diffr.* **2013**, *28* (3), 184−193.

(79) Momma, K.; Izumi, F. VESTA 3 for Three-Dimensional Visualization of Crystal, Volumetric and Morphology Data. *J. Appl. Crystallogr.* **2011**, *44* (6), 1272−1276.

(80) Farrow, C. L.; Juhas, P.; Liu, J. W.; Bryndin, D.; Božin, E. S.; Bloch, J.; Proffen, T.; Billinge, S. J. L. PDFfit2 and PDFgui: Computer Programs for Studying Nanostructure in Crystals. *J. Phys.: Condens. Matter* **2007**, *19* (33), 335219.

(81) Hayashi, S.; Hayamizu, K. Shift References in High-Resolution Solid-State NMR. *Bull. Chem. Soc. Jpn.* **1989**, *62*, 2429−2430.

(82) Massiot, D.; Fayon, F.; Capron, M.; King, I.; Le Calvé, S.; Alonso, B.; Durand, J. O.; Bujoli, B.; Gan, Z.; Hoatson, G. Modelling One- and Two-Dimensional Solid-State NMR Spectra. *Magn. Reson. Chem.* **2002**, *40* (1), 70−76.

(83) Skold, K.; Price, D. *Neutron Scattering*; Academic Press, 1986; Vol. 23A

(84) Sjolander, A. Multi-Phonon Processes in Slow Neutron Scattering by Crystals. *Ark. Fys.* **1958**, *14*, 4310449.

(85) Dovesi, R.; Erba, A.; Orlando, R.; Zicovich-Wilson, C. M.; Civalleri, B.; Maschio, L.; Rérat, M.; Casassa, S.; Baima, J.; Salustro, S.; Kirtman, B. Quantum-Mechanical Condensed Matter Simulations with CRYSTAL. *Wiley Interdisc. Rev. Comput. Mol. Sci.* **2018**, *8* (4), No. e1360.

(86) Laun, J.; Vilela Oliveira, D.; Bredow, T. Consistent Gaussian Basis Sets of Double- and Triple-Zeta Valence with Polarization Quality of the Fifth Period for Solid-State Calculations. *J. Comput. Chem.* **2018**, *39* (19), 1285−1290.

(87) Peintinger, M. F.; Oliveira, D. V.; Bredow, T. Consistent Gaussian Basis Sets of Triple-Zeta Valence with Polarization Quality for Solid-State Calculations. *J. Comput. Chem.* **2013**, *34* (6), 451−459.

(88) Heyd, J.; Scuseria, G. E.; Ernzerhof, M. Hybrid Functionals Based on a Screened Coulomb Potential. *J. Chem. Phys.* **2003**, *118* (18), 8207−8215.

(89) Krukau, A. V.; Vydrov, O. A.; Izmaylov, A. F.; Scuseria, G. E. Influence of the Exchange Screening Parameter on the Performance of Screened Hybrid Functionals. *J. Chem. Phys.* **2006**, *125* (22), 224106.

(90) Kresse, G.; Furthmüller, J. Efficient Iterative Schemes for Ab Initio Total-Energy Calculations Using a Plane-Wave Basis Set. *Phys. Rev. B: Condens. Matter Mater. Phys.* **1996**, *54* (16), 11169−11186.

(91) Blöchl, P. E. Projector Augmented-Wave Method. *Phys. Rev. B: Condens. Matter Mater. Phys.* **1994**, *50* (24), 17953−17979.

(92) Perdew, J. P.; Ruzsinszky, A.; Csonka, G. I.; Vydrov, O. A.; Scuseria, G. E.; Constantin, L. A.; Zhou, X.; Burke, K. Restoring the Density-Gradient Expansion for Exchange in Solids and Surfaces. *Phys. Rev. Lett.* **2008**, *100* (13), 136406.